Universidade de Aveiro Departamento de Física
2018

Jason Earl
Baptista Adams

Análise e Simulação de um Radar Terrestre para a Deteção de Detrito Espacial

Analysis and Simulation of a Ground-based Radar for Space Debris Detection

Universidade de Aveiro Departamento de Física
2018

Jason Earl
Baptista Adams

Análise e Simulação de um Radar Terrestre para a Deteção de Detrito Espacial

Analysis and Simulation of a Ground-based Radar for Space Debris Detection

Dissertação apresentada à Universidade de Aveiro para cumprimento dos requisitos necessários à obtenção do grau de Mestre em Eng. Fisica, realizada sob a orientação de Vitor Bonifácio, Professor Auxiliar do Departamento de Fisica da Universidade de Aveiro e co-orientação de Domingos Barbosa e de Miguel Bergano, Investigadores do Instituto de Telecomunicações.

o júri / the jury

presidente / president

Margarida Facão
Professora Auxiliar da Universidade de Aveiro

vogais / examiners committee

Dalmiro Jorge Filipe Maia
Professor Auxiliar Convidado da Faculdade de Ciências da Universidade do Porto (arguente)

José Miguel da Silva Bergano
Investigador do Instituto de Telecomunicações de Aveiro (co-orientador)

agradecimentos / acknowledgements

Sendo esta a minha última oportunidade de agradecer formalmente a todos os que me ajudaram no meu percurso académico, aproveitá-la-ei para gravar o meu agradecimento pelo passado e ânsia pelo futuro. Um sincero obrigado a todos os que fizeram destes 5 anos um período memorável. Quero, evidentemente, destacar cada um dos meus orientadores por despertarem o meu interesse numa área que jamais pensava aprofundar, o Departamento de Física por estar repleto de personalidades únicas e por fim, a minha mãe por ser inigualável. Avanço para esta nova etapa que rapidamente se aproxima com orgulho do meu desempenho, do meu curso e da minha universidade.

Resumo

Os detritos espaciais, normalmente designados por lixo espacial, têm-se tornado num assunto problemático para a colocação orbital de satélites. Podem causar danos significativos ou até mesmo avariar equipamentos dispendiosos e produzir ferimentos a astronautas em missões espaciais. Agências como a NASA, e mais recentemente a ESA, têm posto em práctica vários programas de rastreio de detritos espaciais recorrendo a uma combinação de telescópios óticos e de rádio. Estes programas actualmente monitorizam cerca de 20 000 detritos maiores que 5 cm. Portugal está a considerar tornar-se membro do programa Space Survey and Tracking (SST) utilizando os Açores como plataforma para a instalação de um radar capaz de detetar detritos no céu entre os 300 – 1800 km. Para investigar as propriedades requeridas para uma infraestrutura espacial deste género, é necessário modelar as respostas do rádio-telescópio. Nesta dissertação apresentam-se os princípios base de radar para as necessidades operacionais propostas tais como noções de Signal-to-Noise Ratio (SNR), Radar Cross Section (RCS) e técnicas de integração de pulsos. Estes princípios foram utilizados para simular o desempenho da antena a instalar nas Flores, Açores, em configuração monostática. O desempenho simulado mostra a capacidade da antena para detetar detrito orbital de tamanho médio e baixo em Low Earth Orbit (LEO). Para efeitos de comparação, o desempenho de um outro radar Açoreano numa configuração mais potente foi também simulado por forma a demonstrar as necessárias capacidades de deteção de objectos em órbita geostacionária (GEO).

Abstract

Space debris, most commonly known as space junk, has become a problematic issue for the orbit placement of satellites. They can cause serious damage or disable costly systems and can potentially produce injuries to astronauts on missions in outer space. Space Agencies like NASA and more recently ESA have put in place several programs for space debris tracking, using a combination of optical and radio telescopes. These programs currently survey almost 20 000 debris pieces larger than 5 cm. Portugal is considering becoming a member of the Space Survey and Tracking (SST) program using the Azores as a platform for the installation of a radar, capable of tracking debris objects in the sky between 300 – 1800 km. In order to investigate the properties required for such a space infrastructure, one needs to model radio telescope responses. This dissertation lays out fundamental radar principles for the operational needs of a radar, notions of Signal-to-Noise Ratio (SNR), Radar Cross Section (RCS), pulse integration techniques are presented along the way. These principles were used for performance simulation of the soon to be installed antenna in Flores, Azores in a monostatic configuration. The calculated values show the antenna's capability in detecting medium to low sized orbital debris in Low Earth Orbit (LEO). For comparison reasons, the performance of another Azorean radar in a more powerful setup was also shown in order to demonstrate the necessary detection capabilities in Geostationary Orbit (GEO).

Contents

List of Figures

List of Tables

Chapter 1

Space Junk

> "The current debris population in the Low Earth Orbit region has reached the point where the environment is unstable and collisions will become the most dominant debris-generating mechanism in the future"
>
> Liou and Johnson, *Science*, 20^{th} Jan 2006

1.1 The Current State of Space Debris

Earth's satellite-based infrastructure is essential for a variety of services which many of us rely on in our daily lives: from meteorology and communications to navigation and reconnaissance. Presently, space debris, or space junk, is one of the main threats to satellites and space based operations. Space debris includes all human-made, non-functioning objects in orbit around Earth, some of which can reenter the planet's atmosphere. The space age began on 4 October 1957 with the launch of the Earth's first artificial satellite, Sputnik 1. Ever since then, the amount of debris in orbit has been steadily increasing, initially due to discarded rocket upper stages and defunct satellites left adrift in orbit, and later due to small bits generated by explosions and even collisions. As of the end of 2017, it was determined that 19 894 bits of space junk were circling our planet, with a combined mass of at least 8135 tons – that equates to more mass than the whole metal structure of the Eiffel Tower.[8] The first step towards the mitigation of such a threat is space surveillance, in order to determine the orbits of most of the objects whose trajectories are close enough to Earth's orbit to pose a threat. We know that most of the artificial material presently orbiting our planet barely consists of operational structures. Most of the orbital debris has accumulated in the main orbits such as Low Earth Orbit (LEO, altitude < 2000 km), Middle-Earth Orbit (MEO, 2000 km < altitude < 31 570 km) and Geostationary Orbit (GEO, 35 586 km < altitude < 35 986 km). An evolution histogram of the number of detected objects among the various tracked orbits is shown in figure 1.1 where LEO has clearly amassed the greatest amount of space junk with a significant increase in the last decade.[1, pp. 10] Therefore, in order to monitor the natural and artificial debris population and to understand their evolution both in short and long term, it is absolutely necessary to complete the models through observations carried out from the

Earth as well as from space. Both to understand the current situation and to observe growth trends. Low-orbiting space debris with a size larger than 10 cm are routinely monitored by

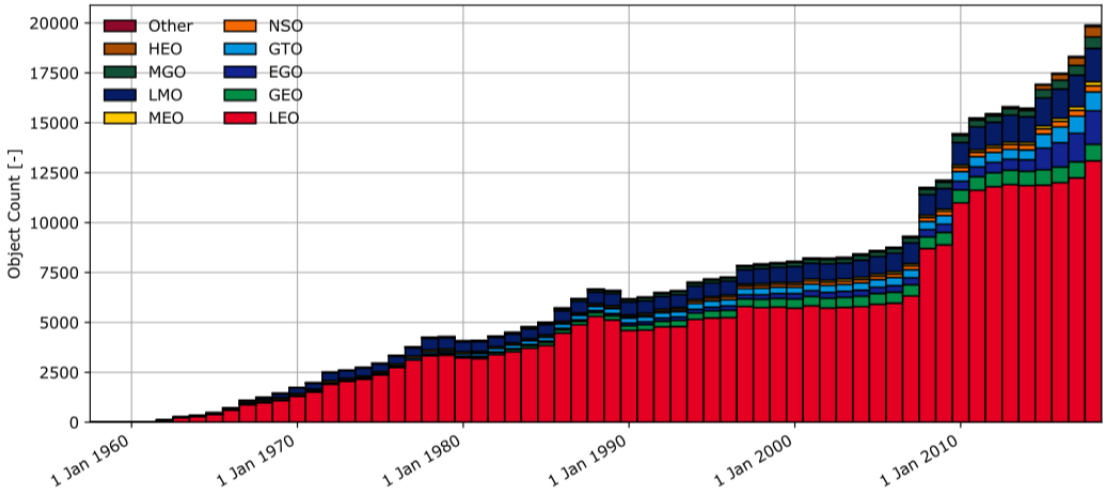

Figure 1.1: Debris objects count evolution in all orbits since the beginning of the space age up to the present. Low Earth Orbit (LEO) has evidently accumulated the greatest amount of debris among the rising tendency of the decade. The remaining initials represent Middle Earth Orbit (MEO), Geostationary Orbit (GEO), LEO-MEO Crossing Orbits (LMO), Extended Geostationary Orbit (EGO), MEO-GEO Crossing Orbits (MGO), GEO Transfer Orbit (GTO), Highly Eccentric Earth Orbit (HEO) and Navigation Satellites Orbit (NSO). Withdrawn from [1, pp. 10].

Unites States (US) based surveillance systems, known as the US Space Surveillance Network (SSN). Though the most common space debris measurement techniques are based on optical and radar ones, the main technique for monitoring them is the latter one. The first one suffers from limitations mainly concerning the dependence on atmospheric conditions and on the illumination of the target by the Sun. Radars, on the other hand, can irradiate at any time, a satellite or space debris in orbit with a microwave beam.[9, pp. 676] A peculiar feature of radar astronomy is the human control over the transmitted signal used to illuminate the target. Radar resorts to coherent illumination whose time-frequency nature and polarisation state are willingly defined by the engineer. The general strategy in radar observations is to send a signal with known characteristics and then, by comparing the echo to the original transmission, some of the target's properties can be deduced.[10, pp. 325] The biggest challenge associated with tracks on smaller debris, is the reacquisition on subsequent passes. Our knowledge of the smaller debris is, in general, indirect or statistical but they are capable of producing significant damage to space systems and they constitute a large fraction of the man-made debris larger than natural space debris.[11, pp. 108] The seemingly unstoppable increase in the number of space debris in low orbits, specifically below 2000 km of altitude in LEO, poses increasingly larger threats to all space-based activities in that region. Due to the high sensitivity and capability to operate independently of the weather, night and day conditions and illumination of the target by sunlight, radar observations have been used to statistically sample the population of space debris in Earth orbit down to a few centimetres in size.[9, pp. 676-677] The number of debris fragments between 1 cm and 10 cm in diameter has been

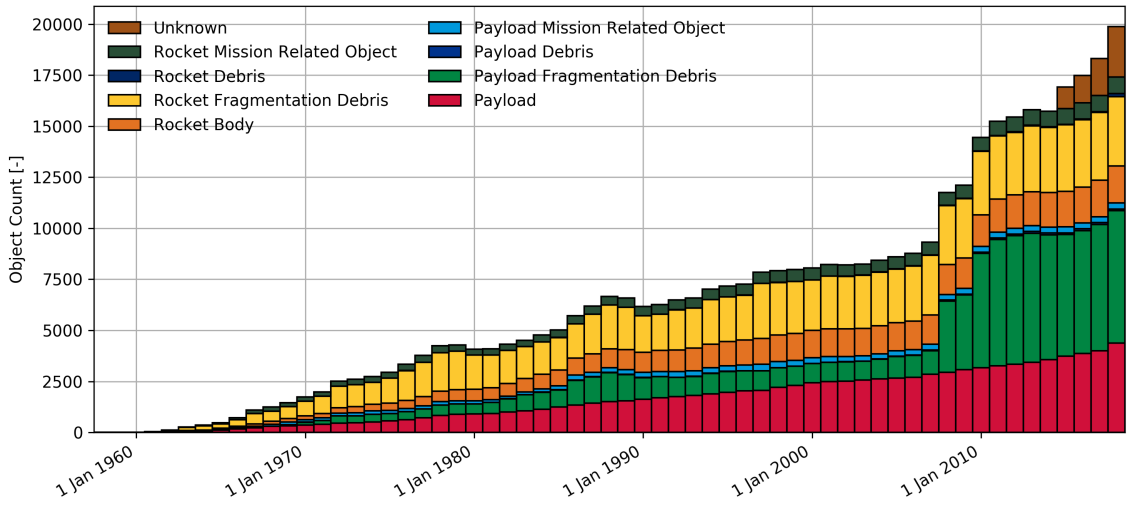

Figure 1.2: Count evolution of the various debris object categories in the near-Earth space environment as a function of time in years. Withdrawn from [2].

estimated at several hundred thousand whereas the population of particles smaller than 1 cm very likely exceeds hundreds of millions. This number is very large and steadily increasing, leaving the satellites in orbit and all the space-based activities exposed to an increasing risk. This has led to research on preventive measures and the implementation of new debris mitigation practices.[9, pp. 676] The number of debris objects regularly tracked by the US SSN and maintained in their catalogue is around 23 000 and the estimated number of break-ups, explosions and collision events resulting in fragmentation is more than 290 where only some were actual collisions — less than 10 accidental and intentional events. The majority of the events were explosions of spacecraft and upper rocket stages and that's why payload and rocket body related fragmentation debris are currently the predominant category of orbital debris as can be seen in figure 1.2.[1, pp. 29][2] Europe still relies on the information provided by the the US SSN for debris environment data between 10 cm and 1 m in LEO and GEO which is then used for its tracking sensors such as the Tracking and Imaging Radar (TIRA) and the ESA Space Debris Telescope (ESASDT).[12, pp. 31] Since the beginning of the space age until the end of 2017, there have been 489 confirmed on-orbit fragmentation events.[1, pp. 42] The primary objective of a future European Space Surveillance System (ESSS) is to equip Europe with the tools needed to guarantee its satellites operational safety. Given that LEO and GEO take up most of the orbital object population, concerning the minimum size of the objects, ESA requirements are 10 cm in LEO and 1 m for further orbits.[12, 32] It is quite logical to think that the ease with which a particular space object can be tracked depends on how big it is — its optical or radar cross section (RCS) — as well as its orbital parameters such as elevation and altitude. The backscattered wave that reflects off the target is accurately detected by a receiving device that may be the same as the transmitting antenna — monostatic radar — or a different one located at a distance of up to several hundred kilometres away — bistatic radar.[9, pp. 676]. Monostatic systems will be the focus throughout the course of this document. The information provided by a radar system can be exploited to validate current

models of debris environment. They can also improve the precision on the knowledge of the orbital parameters of those catalogued debris for which a close encounter with an operational satellite, or a manned spacecraft, is predicted. Finally, they can verify the integrity of big wrecks and update, when possible, the catalogues of big debris currently being tracked.[11, pp. 105-106] The first known collision took place in 1991, when Russia's Cosmos 1934 was hit by a piece of Cosmos 926. Then the french Cerise satellite was struck by a fragment of an Ariane 4 rocket. In 2005, a US upper stage was hit by a fragment of a Chinese third rocket stage. Besides such accidental break-ups, satellite interceptions by surface-launched missiles have been a major contributor in the recent past. By itself, the Chinese FengYun-1C engagement in January 2007 increased the trackable space object population by 25%. Another devastating contribution was the collision between an Iridium satellite and Russian Cosmos-2251 a couple of years later.[13] The numbers from the beginning of 2017 related to the amount of debris objects estimated by statistical models to be in orbit are shown in table 1.1 These numbers

Approximate Size	**1 mm - 1 cm**	**1 cm - 10 cm**	**> 10 cm**
Estimated Number	166×10^6	750×10^3	29×10^3

Table 1.1: Estimated numbers of debris according to their size range.

revealed that the total mass of all space objects in Earth orbit sums up to about 7500 tons.[14] The latest numbers however, as of the end of 2017, revealed that the space debris circling our planet, now has a combined mass of at least 8135 tons.[8] With more than half of those solely residing in LEO.[15]
Given the scarce radar detection coverage of objects under the 10 cm size range and the limited search capability of radars to find and track such objects, confining the search space is critical to their detection. Studies have shown the advantage of multiple site data integration in improving the accuracy of orbit prediction and the possibility of cataloging small debris. The ability to identify likely candidates to provide small debris tracking is a major element in the creation of a small debris catalog.[16, pp. 2-4]

1.2 Space Surveying and Tracking

For many missions, losing a spacecraft because of a space debris object impact is the third highest risk to operations, after the risks associated with launch and deployment into orbit. To avoid collisions of this nature, avoidance manoeuvres must be executed and for that the orbits of objects in space must be well known. This requires a system of sensors typically composed of radars, telescopes and laser-ranging stations, as well as a data center to process all of the acquired observation data. The larger objects (>10 cm) are known to have well-determined orbits and are routinely monitored by the U.S. Space Surveillance Network, which essentially builds the populations between 10 cm and 1 m, with information about the smaller particles being fragmentary and mostly statistical. Since current spacecraft shielding are only capable of protecting against smaller debris, with diameters below about 1 cm, spacecraft manoeuvring is required to avoid collisions with debris larger than 1 cm as it's only

means of protection.[16, pp. 1] As part of the Space Situational Awareness (SSA) Program, the European Space Agency (ESA) is conducting research and developing technologies for systems that can find and track space debris and issue an alert when evasive action may be necessary.
Historically, the National Aeronautics and Space Administration (NASA) and the ESA have carried out measurement and modelling efforts to characterize the LEO debris environment. Even though their models have come to provide a complete description of the debris environment in terms spacial density, flux and such, it should be noted that these models were not intended to catalog debris — create debris elements sets for avoidance — but rather to determine the LEO debris population for risk assessment and spacecraft design.[16, pp. 2]
The objective of a Space Surveillance and Tracking (SST) system is to detect space debris, catalogue debris objects, as well as determine and predict their orbits. The data generated by an SST system can be used to predict hazards to operational spacecraft, such as a potential collision with a debris object, or to infrastructure on ground, such as from a reentering object. Essentially, any SST system can be seen as a 'processing pipeline' for observation data processing acquired by different sensors and provide derived applications and services, typically comprising collision warnings, reentry predictions and risk assessments. The central product of an SST system is an object catalogue, which must contain updated orbit information for all detected objects over a certain size threshold.[17]
The main goal of the SST segment is an updated catalogue, which contains information about the detected objects, such as their orbital parameters and physical properties. For this, several steps must be executed by the SST system:

1. Correlation — verify if the detected object is already a part of the catalogue.
2. Orbit Determination — determine or update the object's orbit from the sensor data.
3. Monitorization — monitor the catalogue data to periodically schedule new observations.

Currently, ESA's SST segment is focusing on integrating and testing SST software. For the present 2017–20 period, committing to a community approach for the SST core software is anticipated, which would help avoid duplication and reduce cost for example.[17] Once a catalogue of all detectable objects that orbit the Earth has been created and is being maintained, the front-end services to be provided by such a software are various and include:

- Orbital parameter catalogue maintenance
- Object owner identification
- Physical parameter estimation
- Atmospheric re-entry prediction
- Fragmentation detection
- Conjunction and collision risk determination

It's envisioned that, given the increase of the space object density in the 1 cm to 10 cm size range, the number of observations and the processing required for them is bound to

increase drastically.[16, pp. 19] On average, 7.3 non-deliberate fragmentations occur in the space environment every year Even though the number is stable for now, the consequential impact of each event is variable. Orbital debris averages 9 km per second and meteoroids average 20 km per second, much faster than a rifle shot in either case. Impacts from debris on space infrastructure can practically deliver the energy equivalent to the explosion of a hand grenade. Such as what is shown in figures 1.3 (a) and (b). To evaluate the actual consequences

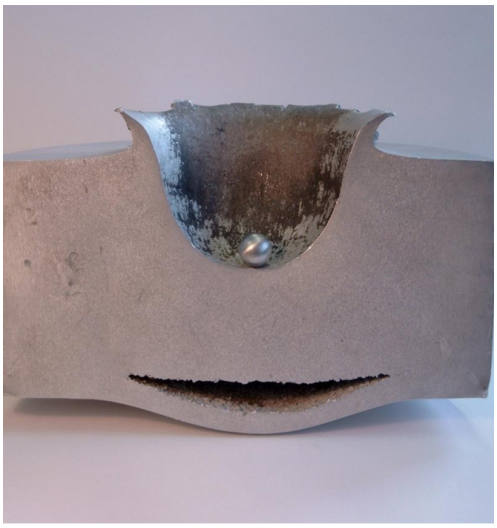

(a) Hypervelocity impact study example. A 1.2 cm diameter aluminium sphere impact at 6.8 km/s on a 18 cm thick block of aluminium.[18].

(b) Consequences of the impact of a 15 g piece of plastic on a block of aluminium at about 24 000 km/h.

Figure 1.3: Potential consequences of hypervelocity impacts.

of such an impact, a collaboration between various entities took place for a project called *DebriSat*. The project's goals were to design and fabricate a spacecraft representative of small modern payloads in the LEO environment — around 60 cm and 50 kg — and conduct a hypervelocity impact test to catastrophically break it up. The test was successfully carried out in April 2014 and the cylindrical projectile used weighed around 0.57 kg and was shot at 6.8 km/s. Posteriorly, all of the resultant fragments as small as 2 mm in size were collected to measure and characterize their physical properties, to then use all the data to improve the satellite breakup models and other space situational awareness applications.[19, pp. 2-3] Many simulation studies have taken place up to the point of accurately predicting the break up behaviour resulting from a hypervelocity impact. One of the main functions of the HyperVelocity Impact Technology is the development of advanced shielding concepts to protect spacecraft in orbit. Much of the shielding development activities have been in support of the International Space Station (ISS), which is to be fully covered with meteoroid and orbital debris shields.[20] NASA developed the Size Estimation Model (SEM), figure 1.4, which shows the size, otherwise known as Estimated Spherical Diameter (ESD), of a detected object as a function of the measured RCS. Though it will be later developed in section 2.2, simply put the RCS is analogous to the target's area "as seen by the radar". Objects with larger

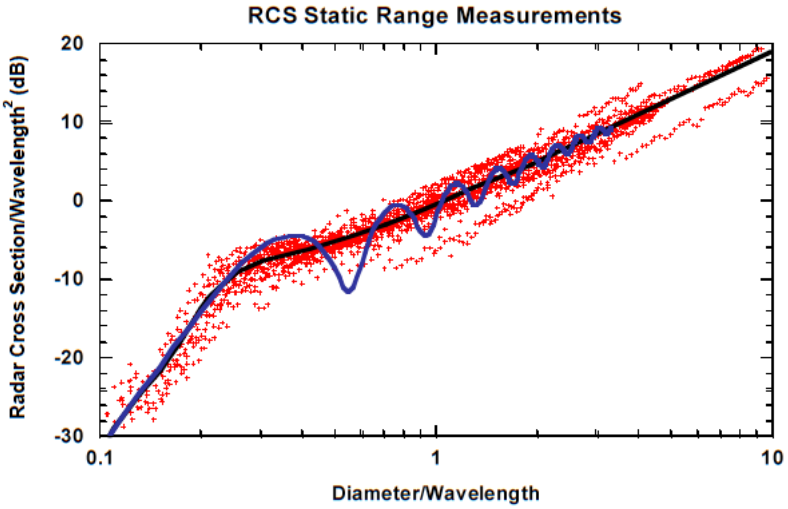

Figure 1.4: NASA Size Estimation Model (SEM) curve — in black — with an overlaid behaviour of a sphere — in blue — and experimental data points used to model the curve — in red asterisks.

RCSs tend to be more easily detectable than those of smaller cross sections. Since the irregular shaped objects cause a great variety of cross section values, an uncertainty in the relation of the RCS to the atual size means that the smallest objects that these systems are capable of cataloguing is also uncertain.[21, pp. 34] The SEM is a RCS-to-ESD mapping function derived from various multi-frequency measurements of around 40 selected debris objects produced by a hypervelocity impact. The pieces were observed at a various frequencies and orientations and RCS probability density functions were derived to characterize the RCS as a function of frequency and object size.[22, pp. 2-3] If the size of an object is known, an estimate of its mass, and thus impact energy, can be made. Given the large identified population of debris between 850–1000 km of altitude[1] and the presence of an almost circular ring comprising mostly of 4 cm sized debris in polar orbit between 1200–1400 km, not only must radars meet the RCS requirements of the SEM, they must also do so over these regions of interest.[16, pp. 6]. Figure 1.5 illustrates the LEO debris population just stated as function of altitude in (a) and as a function of elevation in (b). Curiously, hollow metallic spheres of specified radii were put into orbit to serve as calibration elements for RCS measurements as part of the so called Orbital Debris Calibration Spheres (ODERACS) experiment[2] from NASA. But it was also conducted to serve as an experiment to develop small debris detection and tracking strategies. Since calibration is critical to the characterization of the orbital debris environment. Radars such as the Haystack, the TIRA and the ABM phased-array radars all proved the ability to detect and track the spheres and, consequentially, they had demonstrated the ability to support a small debris catalog.[16, pp. 2] With the increase in the number of objects in space, experts believe that collisions among these objects are soon to become the primary source of new fragments in orbit. However, significant challenges are faced by spacefaring organisations to implement

[1]Mainly small spherical droplets under 2 cm of NaK coolant leaked from reactors that separated from the Russian Radar Ocean Reconnaissance Satellites (RORSATs).

[2]The first experiment of such nature launched 5, 10 and 15 cm spheres at a 250 km altitude.

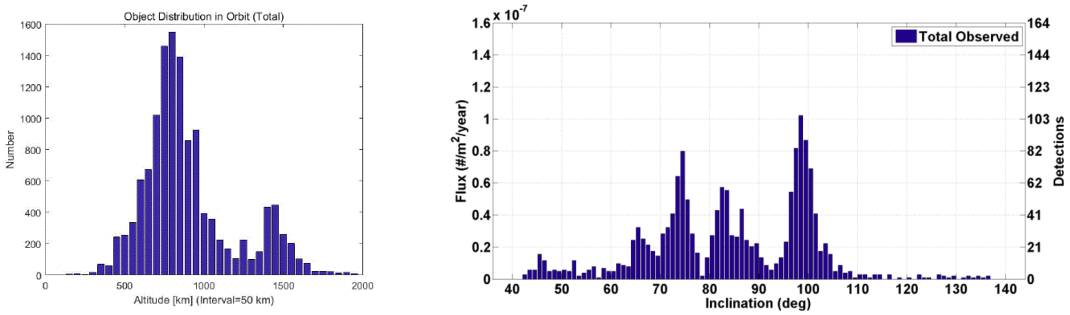

(a) Altitude distribution of space debris objects in the LEO region.[23]

(b) HAX's total reported flux in 2012 versus inclination at 75^{o} East.[5]

Figure 1.5: LEO debris population distribution in terms of altitude (a) and inclination (b).

proposed countermeasures that would mitigate this problem. It becomes necessary to discuss and address acute issues like the current practice in implementing debris avoidance measures, novel concepts for the active removal of debris and the deployment of large constellations of several thousand satellites for telecommunications.[24]

1.3 RAEGE and the Flores Radar

Project RAEGE (for Rede Atlântica de Estações Geodinâmicas e Espaciais) consists of the construction and operation of a network of four Fundamental Geodetic Stations (FGS) in both Spain and Portugal as a part of the developments needed to set up a Very Long Baseline Interferometry[3] (VLBI) Geodetic Observing System (VGOS). The Portuguese will have one in the Açores island of Flores (Lajes). The Spanish will have one in Yebes (Guadalajara), one on the Canary Islands and, even though on Portuguese territory, one in the Açores island of Santa Maria (Saramago).
Taken from the official RAEGE website, figure 1.6 (a) shows a Google Maps^{TM} snapshot of the afore mentioned RAEGE stations in Spain and Portugal. In each of the 4 stations, amongst other equipment, a geodesic radiotelescope of the type VLBI2010 is expected to be installed. Though the antennas of Yebes and Santa Maria have already been inaugurated, the remaining two antennas are yet to be constructed. The major antenna parts for the Flores radar are already contracted and in manufacturing stage while the mechanical parts of the antenna at the Canary islands have already arrived.[7, pp. 3] [26, pp. 50] As of 2015, preliminary work in Flores Island was being conducted after the site of the station had been selected, shown in figure 1.6 (b), in order to characterize the presence of radio-frequency interferences (RFI) at the selected location for the RAEGE station there.[27, pp. 56-57]. As of the latest abstract book from the working meeting of the European VLBI Group for Geodesy and

[3]VLBI is a phenomenally complex and powerful technique used to link radio telescopes around the world to see the sky with great detail. For example, a signal from an astronomical radio source, such as a quasar, is collected at different radio telescope sites on Earth far away from each other preferably. The distance between the radio telescopes can then calculated using the arrival time differences between them from that same radio signal.

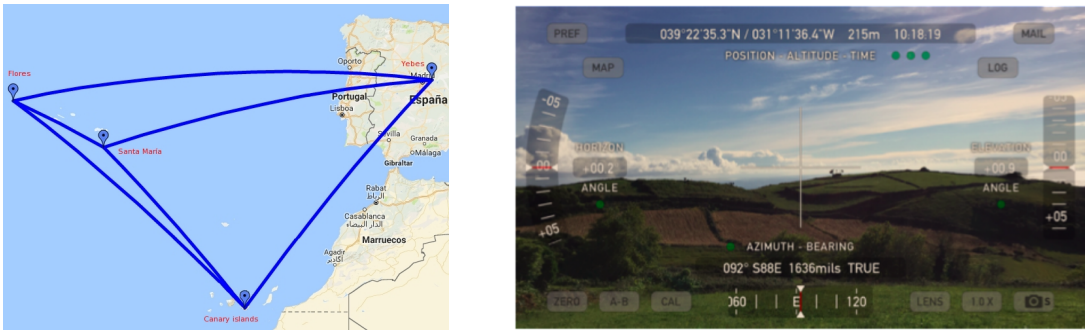

(a) Map of the four fundamental RAEGE stations network.[25]

(b) Selected site for the Flores island RAEGE station construction.[26]

Figure 1.6: Designated locations of the RAEGE fundamental stations.

Astrometry of May 2017, no update was yet done on the Flores antenna's status and Santa Maria's first light had been delayed to the second half of last year (2017).[26, pp. 50] The planned telescope will have a 13.2 m diameter dish and consists of paraboloid, frame, housing and tracking/monitorization device that were engineered to enable a very precise field of view (FoV), i.e. a beam with very low sidelobe levels. When assessing the capability of current debris detection radars to generate orbits of space debris, radar sensitivity and track capability need to be taken into account. Track accuracy is a function of sensitivity, i.e. SNR, of the radar on a given target, while the radar sensitivity is a function of the target's size as measured by its RCS.[16, pp. 4] The most important aspect of this telescope will be its fast mechanics and surface accuracy enabling SST observation modes. In such an observation mode, reliability over the telescope's movement is vital to scan the desired area accurately and allow "stare and chase" observations on low-SNR debris. While its surface accuracy must be guaranteed since any imperfection in the antenna's dish is a potential source of unwanted signal scattering. SST is intended to be the priority observation mode and always available when requested.[7, pp. 1-2] The suitability of the type of antenna planned for the SST radar in Flores with a tracking radar is guaranteed by the Haystack Auxiliary (HAX) radar, operated by the Massachusetts Institute of Technology Lincoln Laboratory (MIT LL) for the NASA Orbital Debris Program Office (ODPO) under an agreement with the U.S. Department of Defence.[7, pp. 4]. The ODPO has initiated and led major orbital debris research activities over the past 38 years, including the development of the first set of NASA orbital debris mitigation requirements in 1995.[19, pp. 1] Short-wavelength ground-based radars have already been used effectively to sample the medium-sized debris population in LEO. Radars generally sample debris in a "beam park" or "stare" mode in which the radar simply stares in a fixed direction — preferably vertically to maximize sensitivity — and debris is counted as it passes through the radar's FoV. By 1995, large amounts of sampling data had been obtained using the Arecibo (λ = 10 cm), Goldstone (λ = 3 cm) and Haystack (λ = 3 cm) radars, though longer wavelength radars had already demonstrated the capability of sampling medium and large debris populations.[21, pp. 40] Figure 1.7 illustrates the range of altitudes and object size detectable by various radars used by the OPDO to sample the debris environment. Increasing

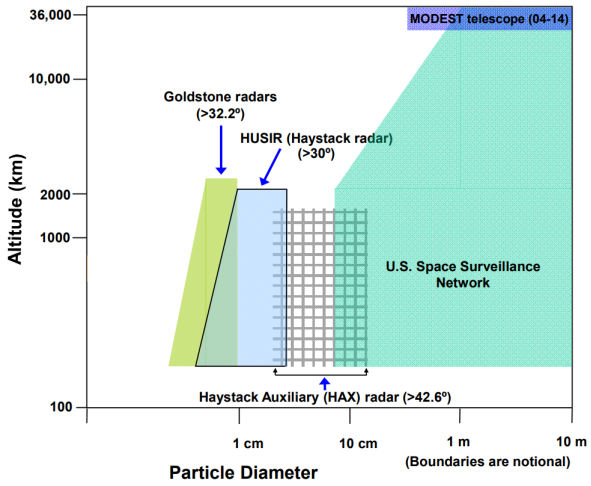

Figure 1.7: Graphical scheme of the various measurement regimes used by the NASA ODPO to describe the near-Earth orbital debris populations. HAX clearly operates at LEO for particle diameters under 10 cm. The effect of the HAX's lower sensitivity compared to the Haystack is evident.

the amount of time that radars spend sampling debris is essentially an issue of allocating the required resources to carry out such additional searches. However, the Haystack, Goldstone and Arecibo radars, which were not designed to detect debris, are expensive to operate and have other users preventing them from being used full-time for debris detection.[21, pp. 41] For these reasons, the HAX Radar was built in 1994 specifically to detect debris. Though not as sensitive as the Haystack, it's larger FoV and lower operating costs allowed data collection on low-altitude, medium-sized debris to be done at a much faster pace and in a much cheaper manner.[21, pp. 42] Track time has a major role in predicting an accurate orbit. The track time available in a fixed beam debris collection mode is a function of the radar's beamwidth. Studies show that if each object is observed every day, for at least 10 seconds, the orbit estimation accuracy would be sufficient for object re-identification at the next crossing.[12, pp. 33] For debris observations, both the Haystack and HAX radars operate in *stare* mode pointed at a specific elevation and azimuth as opposed to *tracking* mode. By operating in stare mode, precise measurements of an object's orbit cannot be obtained due to short transit times of the objects crossing the monitored volume. This operational mode only provides a fixed detection volume for the measurement of debris flux — number of objects per unit of volume per unit of time — as they pass through the FoV.[5, pp. 6] In tracking, or *stare and chase*, mode antennas can follow a target for a greater time allowing for accurate orbit and RCS determinations. It is highly unlikely, though, that the Haystack would ever attempt to operate in a stare and chase surveillance mode given the size and slew rate capability of the antenna. On the other hand, given its larger beamwidth, smaller dimensions and faster mechanics, HAX is very likely to be able to operate in this mode and so is the Flores radar. In this mode it's reasonable to assume that a minimum of 30 seconds of track time could be achieved.[16, pp. 17] HAX is a classical, well understood monopulse tracking radar that was designed to statistically sample objects on LEO that are smaller than those typically tracked and catalogued by the US

Radar Properties	**HAX**	**Flores**
Radar Type	Monopulse Tracking	Monopulse Tracking
Latitude	42.6^o	39.2^o
Antenna Diameter, D	12.2 m	13.2 m
Transmitted Power, P_T	50 kW	50 kW
Average Power, P_{av}	4.89 kW	$\sim$ 4.9 kW
Transmitter Frequency, f_C	16.7 GHz	16.7 GHz
Transmitter Wavelength, λ	1.8 cm	1.8 cm
Pulse Repetition Frequency, f_R	60 Hz	60 Hz
Pulse Width, t_P	1.6384 msec	1.6384 msec
Pulse Bandwidth, f_B	0.61 MHz	0.61 MHz
Gain, G	63.64 dB	
Pulses for integration, n	16	
System Temperature, T	161 K	
System Losses, L	4.5 dB	
SNR_P on 0 dBsm target at 10^3 km	40.6 dB	must be > 41 dB
SNR_P = 3 dB for -40 dBsm target	870 km	must be 900 km

Table 1.2: Radar debris mode operating parameter values for Haystack Auxiliary (HAX) and Flores radars specifications.[5, 6, 7]

SSN and has been operating under the conditions displayed in the second column of table 1.2.[5] This radar is installed at Haystack in Massachusetts at a very close latitude to the one yet to be installed in Flores.[6, pp. 5] The close latitudes of the HAX and Flores radars mean that the detection strategy and object echo statistics will be very similar.[7, pp. 6] Since the HAX radar is a working proxy for space debris tracking radars, the intended operational similarities between the two antennas are shown in table 1.2. It should be noted that in the Flores radar column, the empty entries represent yet undetermined parameter values and the last two rows convey the stipulated values the radar should conform to. While HAX reports less than 3000 objects per year, for Flores a higher SST duty cycle is expected, with at least one full week per month of 8 hour daily observation batches, which equates to 728 hours per year and an object count of around 1500. Extrapolating the HAX's duty cycle to the Flores' one means that if two full weeks per month can be guaranteed, the Flores radar should easily detect over 3000 objects, fitting the requirement of a tracking sensor facility.[7, pp.4]
The continuous monitoring of the LEO environment using highly sensitive radars is essencial for an accurate characterization of the dynamic debris environment. Haystack and HAX have shown that the debris environment can change rapidly. The amount of objects, their combined mass and their combined area have been steadily increasing since the beginning of the space age, leading to the surge of inevitable collisions between operational payloads and space debris.[1, pp. 69] It will be shown that the Flores radar soon to be constructed is a potential candidate for the identification and cataloguing of medium to low sized orbital debris in LEO.

Chapter 2

Theoretical Concepts

2.1 The Radar Range Equation

The radar range equation is a deterministic model that relates received echo power to transmitted power in terms of a variety of system design parameters. It is a fundamental relation used for basic system design and analysis. Since the received signals are narrowband pulses, the received power estimated by the range equation can be directly related to the received pulses amplitude.[28, pp. 54] A radar transmits a pulse with power P_T and detects the echo from a target at a distance R. Assuming isotropic radiation, a spherical symmetry spread occurs and the power per unit area at range R is given by

$$\text{Power Density} = \frac{P_T}{4\pi R^2} \tag{2.1}$$

If the antenna has a gain G and is pointing in the direction of the target, then the power density at the target area would be multiplied by G. Now assume that the target reflects back all the power intercepted by its effective area and that the reflection pattern is isotropic. If the effective area of the isotropic target is σ then the power that it reflects is given by

$$\text{Reflected Power} = \frac{P_T G}{4\pi R^2}\,\sigma \tag{2.2}$$

Since the power is reflected isotropically, the reflected power density back at the radar is

$$\text{Reflected Power Density} = \frac{P_T G}{4\pi R^2} \times \frac{\sigma}{4\pi R^2} \tag{2.3}$$

So if the radar's receiving antenna has an effective area A_e, then the power received by the antenna is given by

$$P_R = \frac{P_T G}{4\pi R^2} \times \frac{\sigma}{4\pi R^2} \times A_e \tag{2.4}$$

The right hand side of the equation 2.4 has been written as a product of 3 factors representing 3 distinct physical products. The previous rationale assumes an isotropic reflecting pattern from the considered target with area σ, which is a rare occurrence since most targets are not isotropic. To use the radar equation we'll replace each real target with an isotropic target

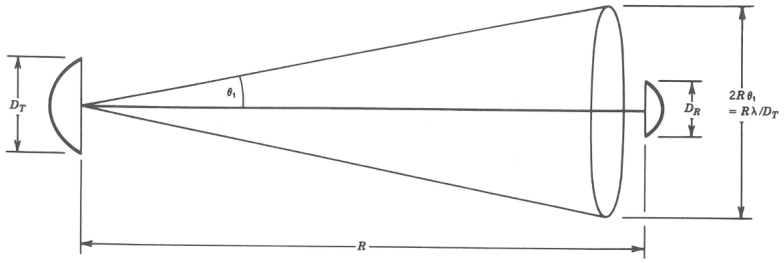

Figure 2.1: Schematic illustration of the illumination geometry between two parabolic antennas at a distance R from each other. Withdrawn from [3, pp. 9]

and change the area of the isotropic target until it produces the same return power as the original target. Thus σ is the area of a that reflects back isotropically and would have caused the same return power as the original target. It is called the Radar Cross Section (RCS) and it's quite different from the physical area of a real target. Furthermore, most targets exhibit different RCS's at different aspect angles and at different frequencies.[3, pp. 5] This will later be developed in section 2.2.

If we think of an antenna as a receiving area interrupting a power flux S and yielding a received power P_R, the effective area is a function of its direction $\hat{n}$ (measured with respect to the antenna axis). The range of directions over which the effective area is large is the antenna beamwidth. From laws of diffraction we extract that an antenna of size D has a beamwidth in the order of λ/D. On the other hand, as a transmitter the same antenna would have a gain $G(k)$ in a direction $\hat{n}$ which is the ratio between the power flux $S(k)$ that would be measured at the some large distance and the power flux from a hypothetical isotropic radiator, measured at the same distance.[29, pp. 9] Most radars use the same antenna for transmitting and receiving, known as a monostatic configuration, and there's a relation between the gain of an antenna when transmitting and its effective area when receiving that we will arrive at in a moment. Conservation of energy requires that the integral of $S(\hat{n})$ over the whole sky, i.e., 4π solid angle, must equal the transmitted power P_T so that

$$\int_{4\pi} G(\hat{n})\, d^2\Omega = 4\pi$$

Most antennas concentrate the radiation into a single principle beam of effective solid angle Ω_0. This condition may be approximated by

$$G = \frac{4\pi}{\Omega_0} \tag{2.5}$$

Take a horizontally transmitting parabolic antenna such as the one shown in figure 2.1 and that, in this layout, the antenna generates wavefronts parallel to the line uniting each of the antenna's edges. If the antenna's beam for some reason is set to be tilted upwards at an angle θ, pointing in a more elevated direction, the additional distance travelled by the wave from the bottom edge of the antenna to maintain a wavefront in the desired direction is $D\sin(\theta) \approx D\,\theta$. With D being the antenna's diameter and θ being very small to validate the

approximation. If this additional distance happens to be $\lambda/2$, where λ is the wavelength of the radar signal, then the radiation from the two edges of the parabolic antenna cancel each other out by being out of phase. Which by itself suggests that in the direction

$$\theta_1 = \frac{\lambda}{2D} \tag{2.6}$$

the overall radiation is significantly weaker than at the original $\theta = 0$. Let's also consider that this antenna emits an isotropic radiation pattern inside a cone of radiated power defined by a positive and negative tilt of θ_1, i.e, $|\theta| < \theta_1$, and is zero outside this cone. Thus, at a distance R from a transmitting antenna of diameter D_T, simple trigonometry helps affirm that the power is then evenly distributed within a cone of $2R\theta_1$. Substituting equation 2.6 into it we get $R\lambda/D_T$. If a receiving parabolic antenna with a diameter of D_R is placed at this distance R, then the received power will be the area that D_R intercepts.

$$\frac{P_R}{P_T} \approx \frac{D_R^2}{(R\lambda/D_T)^2} \tag{2.7}$$

Converting from diameter to area we get

$$\frac{P_R}{P_T} \approx \frac{16A_RA_T}{\pi^2(R\lambda)^2} = 1.62\frac{A_RA_T}{(R\lambda)^2}$$

The factor 1.62 comes from the simplifying assumptions that were made, the exact factor is in fact 1.

$$\frac{P_R}{P_T} = \frac{A_RA_T}{(R\lambda)^2} \tag{2.8}$$

On the other hand, it was shown that the received and reflected power by an area $A_R = \sigma$ is given by equation 2.2. Equating 2.8 to 2.2 we finally arrive also at

$$A_T = \frac{\lambda^2 G}{4\pi} \tag{2.9}$$

In a real situation, the radio telescope's transmitting area A_T, otherwise known as A_e, is related to its geometrical area through the efficiency ϵ:

$$A_T = \varepsilon A_{geo} \tag{2.10}$$

Another form of the radar equation is the Signal-to-Noise Ratio (SNR) as a function of target distance or range, R. In order to develop this form it'll be helpful to define what a signal in fact is so that it can be shown later that the equation is universal for all signals.[3, pp. 7] If we assume the signal to be a train of coherent radio frequency pulses, at a carrier frequency f_C, such as the one shown in figure 2.2, a nearly optimal receiver for the detection of the pulse train simply comprises of a bandpass filter[1] (BPF) "matched" to the single-pulse width, t_P,

[1] A bandpass filter essentially consists of a high-pass and a low-pass filters combined as to create a range, or "band" of allowed frequencies. The size of this band is known as the bandwidth.

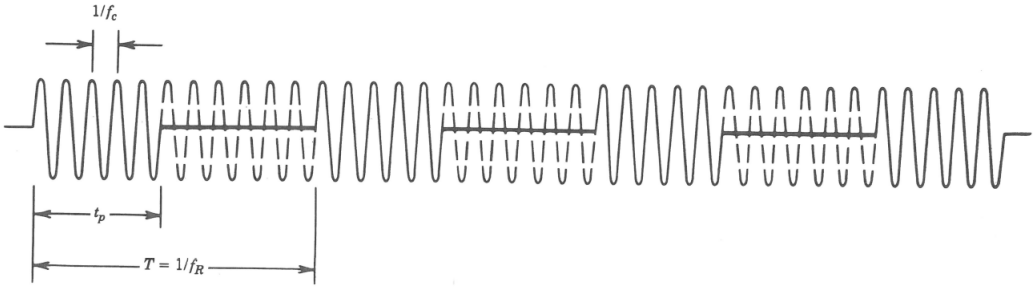

Figure 2.2: A coherent Pulse Train can be given by a periodically interrupted sinusoidal wave. Where f_C is the carrier frequency, t_P is the pulse width and f_R is the pulse repetition frequency. It should be noted that t_P and T are not necessarily Withdrawn from [3, pp. 9]

followed by a synchronous detector[2] and an integrator. This will be further developed in subsection 2.4.1. Simply explained, the bandpass filter with a rectangular response over the bandwidth, f_B, is a good representative of a filter matched to a single-pulse of duration t_P, if the bandwidth is related to the pulse duration as

$$f_B = \frac{1}{t_P} \tag{2.11}$$

The thermal noise power N after such a filter is given by equation 2.12.

$$N = N_F k_B T f_B = N_0 f_B \tag{2.12}$$

The terms $k_B T f_B$ together represent the so called thermal noise from an ideal ohmic conductor, where k_B is the Boltzmann constant, T is the standard temperature of 290 K and f_B is the bandwidth of the receiver. To account for the additional noise introduced by a practical (non-ideal) receiver, the thermal noise expression is multiplied by the noise figure N_F of the receiver, defined as the noise out a practical receiver to the noise out of an ideal receiver.[30, pp. 1.11]. Lastly, N_0 is known as the noise power spectral density[3].

For a received signal to be detectable it has to be larger than the receiver noise by a factor denoted as SNR_P. SNR_P is the Signal-to-Noise ratio when only one pulse is returned from the target, also called the single-pulse or single-sample SNR, and all three notations will be referred to throughout this document.

Having deduced both the noise power and the signal power, it is now possible to express the radar equation in terms of the desired signal-to-noise ratio:

$$\frac{P_R}{N} = \text{SNR}_P = \frac{P_T G^2 \lambda^2 \sigma}{(4\pi)^3 R^4 N_F k_B T f_B} \tag{2.13}$$

Since the target is usually illuminated for a relatively long period of time T_i, and the number of pulses that can be used is n, where

$$n = T_i f_R \tag{2.14}$$

[2] A device that performs frequency conversion operations into a complex representation $I + jQ$ thus recovering phase and magnitude information present in the modulated signal. Also referred to as an I/Q demodulator or coherent detector.[30, pp. 6.31]

[3] The power spectral density of a signal describes its power per unit of frequency behaviour in W/Hz.

and f_R is the pulse repetition frequency (PRF). Though it will later be further developed in section 2.4.1, the SNR of n coherently integrated pulses is essentially n times the SNR of a single-pulse. That is:

$$\text{SNR} = n\ \text{SNR}_P = \frac{nP_T G^2 \lambda^2 \sigma}{(4\pi)^3 R^4 N_F k_B T f_B} \tag{2.15}$$

We already know that the power P_T is the peak power of the transmitted radar pulse. But the average power P_{av} is another measure of the ability of a radar to detect targets so it can be inserted into the radar equation using the relation

$$P_{av} = P_T f_R t_P = P_T \frac{n}{T_i f_B} \tag{2.16}$$

So the new version of the radar equation becomes:

$$\text{SNR} = \frac{P_{av} T_i G^2 \lambda^2 \sigma}{(4\pi)^3 R^4 N_F k_B T} \tag{2.17}$$

The previous equations 2.15 and 2.17 assumed coherent integration of the received signal over the entire illumination time, T_i. If this isn't the case, then the radar equation should be modified to include an integration loss or efficiency factor, as we will later discuss. It is customary to include all the possible losses in one coefficient L, greater than unity, which should appear in the denominator of the equations 2.15 and 2.17 given that a loss term should be added to account for the many ways that loss can occur in radar[4]. This factor might be quite large and if the system loss is ignored, then very large errors could influence the radar predictions. Finally the radar equation becomes:

$$\text{SNR} = \frac{P_{av} T_i G^2 \lambda^2 \sigma}{(4\pi)^3 R^4 N_F k_B T L} \tag{2.18}$$

On the other hand, if the previous rationale would assume noncoherent integration on n samples, then an integration efficiency should be accounted for through a factor that somehow depends on the number of integrated pulses. We will eventually deduce, in section 2.4, this term called Noncoherent Gain, $G_{nc}(n)$. And since the surface and atmosphere of the Earth can drastically affect the propagation of electromagnetic waves and change the coverage and capabilities of a radar it also suggests that these propagation effects should be accounted for by a factor[5] F in the numerator of the radar equation.[30, pp. 1.12] The final form of the equation would take the form:

$$\text{SNR} = \frac{P_{av} G^2 \lambda^2 \sigma F^4 G_{nc}(n)}{(4\pi)^2 k_B T N_F f_R R^4 L} \tag{2.19}$$

Equation 2.19 applies for a radar that observes a target long enough to receive n pulses. Therefore it applies for a radar where the time on the target T_i is equal to $\frac{n}{f_R}$. The radar

[4]Losses such as those associated with reception and transmission, atmospheric absorption, attenuation and the erroneous assumption that the radiation pattern is uniform over the whole antenna beamwidth.[3, pp. 13][4]

[5]Called the propagation factor, it mainly accounts for losses due to path propagation and is usually expressed to the fourth power.[30, pp. 26.2]

equation is our main source of information on the expected return signal and SNR.[3, pp. 4]. The target's range velocity and bearing can be measured very accurately when the return SNR is high. A contributing factor for this is the size of the target as seen by the radar, known as the Radar Cross Section, σ.

2.2 Radar Cross Section

An object exposed to an electromagnetic wave disperses incidente energy in all directions. This spatial distribution of energy is called scattering and the object itself is called the scatterer. The energy scattered back to the source of the wave, or backscattered, constitutes the radar echo of the object. The intensity of the echo is described explicitly by the radar cross section (RCS) of the objet. Early papers on the subject called it echo area or effective area.[30, pp. 14.2] It's essentially a measure of how detectable an object is with radar and is a function of various parameters such frequency, direction of incidence target shape and polarisation.[31, pp. 141] Remember that the incident power density at the target is given by equation 2.1 and that the backscattered power density at the transmitter, if that power resulted from an isotropic radiation from the target, is 2.3. The radar cross section (RCS) of a target is the fictional area over which the transmitted power density must be intercepted to collect a total power that would account for the received power density, that is σ must satisfy equation 2.2, i.e,

$$\sigma = 4\pi R^2 \frac{\text{Reflected Power Density}}{\text{Transmitted Power Density}} \tag{2.20}$$

This definition is usually written in terms of the electric field amplitude[30, pp. 14.2] Also, in order to make the definition dependent only on the target characteristics, R is eliminated by taking the limit as the range tends to infinity. Thus, the formal definition of the radar cross section becomes:

$$\sigma = \lim_{R\to\infty} \left(4\pi R^2 \frac{|E_R|^2}{|E_T|^2} \right) \tag{2.21}$$

where E_T is the electric field strength of the incident wave impinging on the target and E_R is the electric field strength of the reflected wave at the radar. Although the vast majority of targets do not scatter uniformly, this definition assumes that they do. This allows one to calculate the scattered power density on the surface of a large sphere of radius R centered on the scattering object. R is typically taken to be the distance from the radar to the target. The limiting process used in equation 2.21 is not always an absolute requirement in both measurement and analysis, the radar receiver and transmitter are taken to be in the far-field of the target, and at that distance, the scattered field E_S decays inversely to the distance R. Thus the R^2 term in the numerator cancels out with the identical and implicit term in the denominator. Consequently, the dependence of the RCS on R and the need to form the limit, usually disappears.[30, pp. 14.2] The radar cross section of real targets cannot be effectively modelled as a simple constant. In general, RCS is a complex function of aspect angle, frequency and polarization, even for relatively simple scatterers. For example, a conducting trihedral corner reflector is often used as a calibration target in field measurements and its

RCS, when viewed along its axis of symmetry (looking into the corner) can be determined theoretically and is shown in the following equation 2.22.[28, pp. 67]

$$\sigma = \frac{12\pi a^4}{\lambda^2} \tag{2.22}$$

Thus it can be seen that the RCS increases with the decrease of the carrier wavelength. Which is the same as saying that it increases with the increasing frequency. On the other hand, at least one frequency- and aspect- *independent* scatterer exists, and that is the RCS of a conducting sphere of radius a is a constant πa^2, provided $a \gg \lambda$. It's independent of aspect angle because of its spherical symmetry.[28, pp. 68] For a multiple-scatterers target, if the number of scatterers is greater than two and the spacing between them is larger than a couple of wavelengths, then the total cross section becomes strongly dependent on the aspect angle and a complex scattering pattern arises.[3, pp. 27] A simple example of frequency and aspect

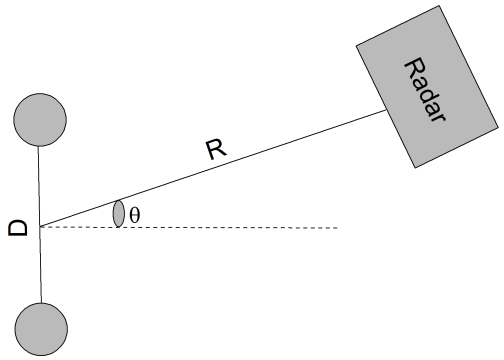

Figure 2.3: Schematic diagram for determining relative RCS of a simple "dumbbell" shaped two point target illustrating a 360^o rotation of the radar around the target.

angle dependence is the two-scatterer "dumbbell" target of figure 2.3. If the radar-target range, is much greater than the separation, i.e. $R \gg D$, the range to each of the two scatterers in the target from the radar is approximately given by equation 2.23.[28, pp. 68-69]

$$R_{1,2}(\theta) \approx R \pm \frac{D}{2}\sin(\theta) \tag{2.23}$$

Assuming a signal of the form $y(t) = a\, e^{j2\pi ft}$ is transmitted, the return echo will take the form of $y_R(t) = a\, e^{j2\pi f(t-2R_{1,2}(\theta)/c)}$. In other words, after the signal is transmitted, the composite echo signal would have an additional phase shift corresponding to the travelled distance of the wave from its source to each scatterer in the target and back, namely $2R_{1,2}(\theta)$. The RCS is proportional to the power of the composite echo. Taking the squared magnitude of the composite echo voltage, $|y_R(t)|^2$, we arrive at the following equation 2.24.

$$\sigma = 4a^2|\cos(\pi f D\sin(\theta)/c)|^2 = 4a^2|\cos(\pi D\sin(\theta)/\lambda)|^2 \tag{2.24}$$

Which shows that RCS is a periodic function of both radar frequency, f, and aspect angle, θ. The larger the scatterer separation in terms of wavelengths, the more rapidly RCS changes

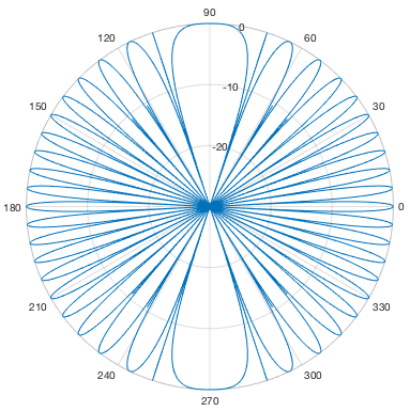

(a) Dumbbell polar RCS plot with 0.1º sampling step.

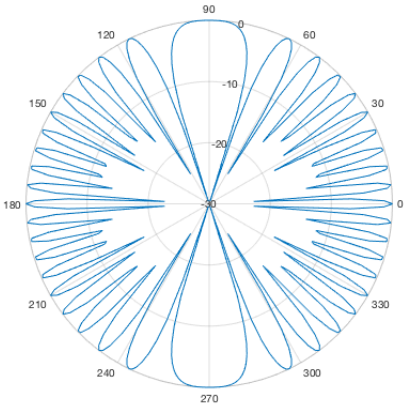

(b) Dumbbell polar RCS plot with 1º sampling step.

Figure 2.4: Polar plot comparison of the resulting dumbbell target RCS for distinct a sampling steps.

with those quantities. An attempted reproduction of the bibliography's results, with $D = 10\lambda$ and $R = 10\ 000\ D$, suggests that the figures can be misleading. It might be interesting to note that the graphs in figure 2.4 show that by simply changing the iteration's, or sampling, step we obtain drastic visual changes in the respective plots. Namely, if the limits of the polar plots are not set to include the function's minimum values, distinct "peaks" that seem to go over the normalized function's maximum value of zero show up such as the ones on either side of the largest main lobes in figure 2.4 (a). Though there is one element that keeps unchanged, which is the four-fold symmetry present in each of the polar plots if and only if the sampling step is linearly spaced and is also "angularly symmetrical" (p.e. that the points 0º and 180º are evaluated or 90º and 270º and so forth). The consulted bibliography's (namely [3] and [28]) figures suggested that the four-fold symmetry was not present by using the $linspace(a, b, n)$ function to create the independent variable θ. Although this function produces n linearly space points between the interval $[a, b]$, it does not evaluate "angularly symmetrical" points except under very specific conditions. The slight difference in the θ vectors created was enough to produce noticeable changes to the figure's output given the suggested logarithmic nature of the final calculation. Since all the RCS values are normalized and then are translated into decibels, each time the normalized function approaches zero, the logarithmic function tends do negative infinity, $-\infty$. The finer the sampling step, the lower negative values the plotted functions hit. Such as what is seen in figure 2.5 (a), where a 0.1º sampling step leads to a minimum of about -70 dB in the function while a sampling step of 1º takes the function to minimums of about -30 dB. Therefore, one should point out that the analysis should stop at the normalization process in order to consistently constrict the limits of each plot between [0, 1] relative units instead of $]-\infty, 0]$.
Considering that a complicated pattern results from fairly simple and idealised targets, it's obvious that any real-world multiple-scatterers target will yield an even more complicated pattern. For such a target it makes sense to abandon the deterministic approach and to treat the RCS, σ, as a random variable because when there is motion relative to the radar, the angle

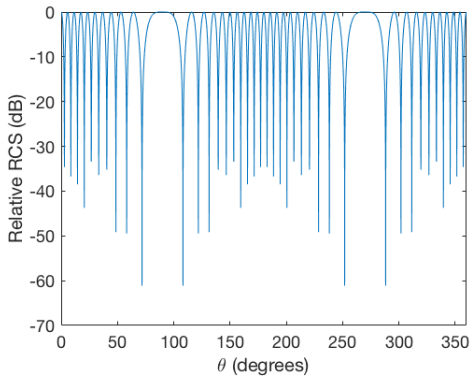

(a) Dumbbell RCS plot with 0.1º sampling step

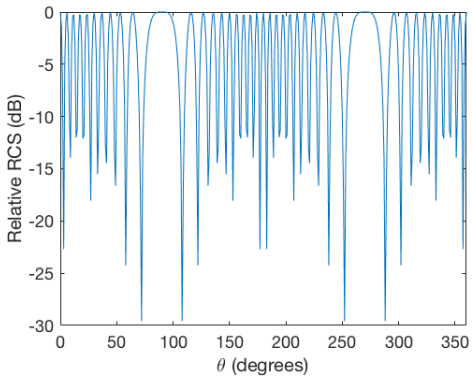

(b) Dumbbell RCS plot with 1.0º sampling step

Figure 2.5: Linear plot comparison of the resulting dumbbell target RCS for distinct sampling steps.

of incidence changes and therefore yields different RCS values. It becomes more practical to describe the targets in terms of the probability density function (PDF) of their RCS, σ. When the target is constructed from many independently positioned scatterers, the PDF of its σ can usually be described by a Rayleigh PDF, also called *exponential* PDF.

$$p_1(\sigma) = \begin{cases} \frac{1}{\overline{\sigma}} \exp\left(\frac{-\sigma}{\overline{\sigma}}\right) & \text{, if } \sigma \geq 0 \\ 0 & \text{, if } \sigma < 0 \end{cases} \tag{2.25}$$

where $\overline{\sigma}$ is the average RCS. It can be simply represented by

$$p_1(\sigma) = \frac{1}{\overline{\sigma}} \exp\left(\frac{-\sigma}{\overline{\sigma}}\right), \qquad \sigma \geq 0$$

Since σ is linearly related to the received power, equation 2.25 is the power version of the Rayleigh PDF.[3, pp. 28-29] To convert it to the amplitude version we first note that, ignoring constants, the amplitude A is related to power, hence to σ, as

$$\sigma = \frac{A^2}{2}$$

therefore we can obtain a second function through

$$p_2(A) = \frac{p_1(\sigma)}{|dA/d\sigma|_{\sigma=A^2/2}}$$

which yields, when $A_0^2 = \overline{\sigma}$:

$$p_2(A) = \frac{A}{A_0^2} \exp\left(\frac{-A^2}{2A_0^2}\right), \qquad A \geq 0 \tag{2.26}$$

Where A_0 is the most probable A. The Rayleigh or exponential distribution can be seen as a special case, when $k = 1$, of a distribution family called *chi-square*, more specifically a

chi-squared distribution of degree 2, and described by the PDF in equation 2.27.

$$p_3(\sigma) = \frac{k}{(k-1)!\,\overline{\sigma}} \left(\frac{k\sigma}{\overline{\sigma}}\right)^{k-1} \exp\left(\frac{-k\sigma}{\overline{\sigma}}\right) \tag{2.27}$$

So as we just saw, the radar range equation is used to estimate the average RCS and one of a variety of PDFs is used to describe its statistical behaviour since not all targets are well-described as an ensemble of equal-strength scatterers.[28, pp. 72] In the case of a target consisting of multiple scatterers, if the number of scatterers is larger than two and the spacing is longer than a few wavelengths, then the total cross section becomes strongly dependent on aspect angle and a very complicated scattering pattern arises. Take, for example, the total cross section of five isolated spherical scatterers located in a plane away from the observer at a distance z, at the Cartesian coordinates $(2, 0, z)$, $(1, 3, z)$, $(-1, 1, z)$, $(-3, -1, z)$ and $(0, -2, z)$. If we assume a wavelength of λ=0.28 in the same units, choose spheres to simplify the analysis and carry out a 360º scan around the hypothetical plane just described using equation 2.24, the resulting RCS values are plotted in figure 2.6. Spheres are chosen since they exhibit no dependence of σ_n on the aspect angle and can be considered the same size as to guarantee $\sigma_n = \sigma_1$. If a histogram count of the RCS value occurrences is performed, the result is

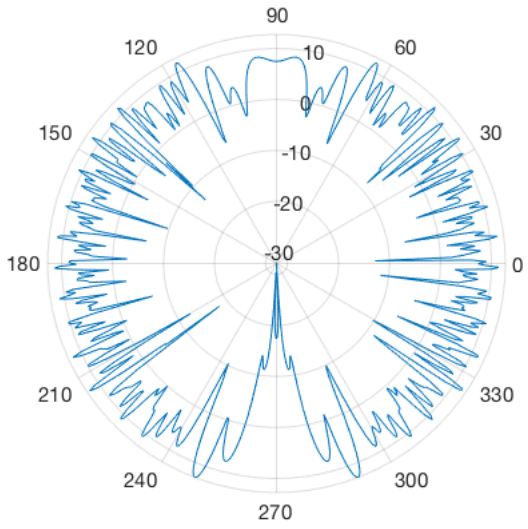

Figure 2.6: Polar plot of one 360º scan around a plane with 5 pre-allocated points evenly illuminated with a λ=0.28 at a distance of z=25 (in the same units) where the sampling step used was 0.1º. The magnitude of the RCS values decreases towards the center and is given in dB while the value of the angle increases in a counter-clockwise fashion.

plotted in figure 2.7 in which the theoretical Rayleigh distribution was overlaid to show the accurateness of the statistical model. The fit might not be obvious at first but it is worth to mention that the $p(\sigma)$ of each histogram bar corresponds to the cumulative sum of the Rayleigh PDF up to the edge of each bar. For this reason these values where overlaid on the graph in the form of asterisks indicative of the area under the Rayleigh PDF curve between each bar edge. Namely, the first histogram bar shows the value of $p_1(0 \leq \sigma < 1.5)$ while the

second bar shows the value of $p_1(1.5 \leq \sigma < 3.0)$ and so forth. The complicated behaviour

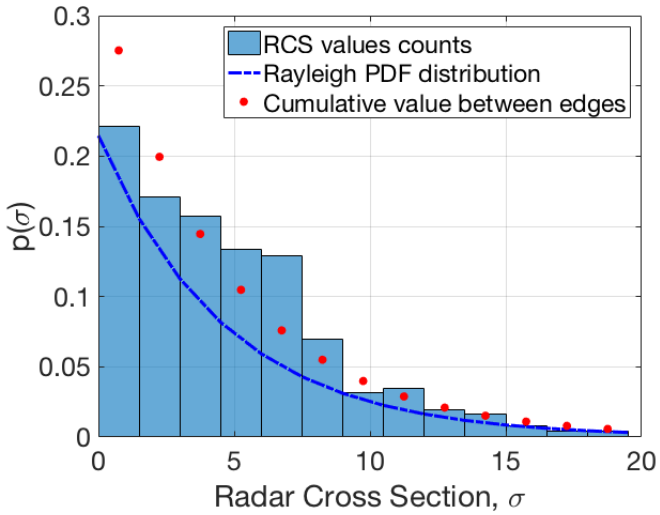

Figure 2.7: Histogram count of the RCS occurrences in each value interval with the Rayleigh PDF of equation 2.25. It should be noted that the value of each bar should be close to the cumulative sum of the curve in the interval that the bar occupies, represented by red asterisks in the figure.

observed for even moderately simple targets leads to the use of a statistical description of a target's radar cross section. This means that the RCS, σ, of the scatterers within a single resolution cell is considered to be a random variable with a specified *probability density function* (PDF). The general radar range equation deduced in the previous chapter is used to estimate the mean RCS, $\overline{\sigma}$, and one of a variety of PDFs are used to describe the statistical behaviours of the RCS. If we first consider a target consisting of a large number of individual scatterers randomly distributed in space, each with its own, but fixed, RCS, it can be assumed that the phase echoes from the various scatterers is a random variable distributed between 0 and 2π. The central limiting theorem guarantees that, under these conditions, the real and imaginary parts of the composite echo can each be assumed to be independent, zero-mean Gaussian random variables (RV) with the same variance.[28, pp. 71] The PDF shape of the RCS directly affects detection performance and many radar targets are not well modelled as an ensemble of equal-strength scatterers, so many other PDFs have been advocated and used to describe them[6].[28, pp.72] Consider that the radar evenly illuminates an area in which n reflectors are inserted. The common illumination that all targets share means that the antenna beam sees all the n reflectors and, because of the extended duration of the transmitted signal, they all contribute to the received signal with a given delay. The difference in the ranges to the various reflectors is expressed in the relative phases of the reflected signals, and the differences in their sizes affects the magnitude of the individually reflected signals.[3, pp. 30] Furthermore, assume also that because of the roughness of the target area, the range differences to the various reflectors are much larger than the wavelength of the transmitted signal. Because of the modulo 2π nature of the phase term, it is therefore reasonable to assume that the phase of

[6]Some of them include the Weinstock, Weibull, Log-normal, Rician, Chi-square of degree 2 or 4, etc.

the returns from the various reflectors will be a random variable with a uniform PDF between 0 and 2π radians.[3, pp. 30] Expressing the signal reflected from the target as a sum of n signals with a common central phase and frequency and with individual amplitudes and additional phases we obtain:

$$s_R(t) = Re\left(e^{j\omega_C t + j\phi_0} \sum_{k=1}^{n} a_k e^{j\phi_k}\right) \tag{2.28}$$

The sum in equation 2.28 describes the complex envelope of the returned signal and will be termed

$$u = r\, e^{j\theta} = \sum_{k=1}^{n} a_k e^{j\phi_k}$$

which can also be written as

$$u = \sum_{k=1}^{n} a_k \cos(\phi_k) + j \sum_{k=1}^{n} a_k \sin(\phi_k) \tag{2.29}$$

We will simplify the assumption that all scatterers contribute equally by choosing

$$a_k = a$$

Thus equation 2.29 becomes

$$\frac{u}{a} = \sum_{k=1}^{n} \cos(\phi_k) + j \sum_{k=1}^{n} \sin(\phi_k) = X + jY \tag{2.30}$$

Since ϕ_k is distributed evenly between 0 and 2π, both $\cos(\phi_k)$ and $\sin(\phi_k)$ have a zero mean. For a large number of pulses n, the central limit theorem is satisfied, and both X and Y defined in equation 2.30 become Gaussian distributions with zero mean and a variance of $\cos(\phi_k)$. Thus

$$Var\ Y = Var\ X = n \int_0^{2\pi} \frac{1}{2\pi} \cos^2\phi\, d\phi = \frac{n}{2} \tag{2.31}$$

We also know that X and Y are uncorrelated random variables (RV)[7] since from equation 2.30

$$E\{XY\} = 0 = E\{X\}E\{Y\}$$

Being uncorrelated and Gaussian implies that X and Y are also independent. We can now obtain the PDFs of r and θ. We note that

$$\left(\frac{r}{a}\right)^2 = X^2 + Y^2 \qquad\qquad \theta = \arctan\frac{Y}{X}$$

where X and Y are independent Gaussian RV with zero mean and variance $n/2$. The joint PDF of X and Y is given by

$$p(X,Y) = p(X)\ p(Y) = \frac{1}{n\pi} \exp\left(\frac{-(X^2+Y^2)}{n}\right) \tag{2.32}$$

[7]Two real-valued RV are said to be uncorrelated if their covariance (i.e. the mean value of the product of the deviations of two variates — a variate is defined as the set of all RV that obey a given probabilistic law — from their respective means) equals zero

yielding

$$p(r) = \frac{2r}{na^2} \exp\left(\frac{-r^2}{na^2}\right), \qquad r \geq 0 \tag{2.33}$$

and

$$p(\theta) = \frac{1}{2\pi}, \qquad 0 \leq \theta < 2\pi \tag{2.34}$$

Using the transformations

$$A = r\sqrt{2} \qquad A_0^2 = na^2$$

in 2.33, we finally get

$$p(A) = \frac{A}{A_0^2} \exp\left(\frac{-A^2}{2A_0^2}\right), \qquad A \geq 0 \tag{2.35}$$

which is the Rayleigh PDF (for amplitude) appearing in 2.26. Our analysis assumed equal contributions from all the scatterers, relation 2.2, but it can be shown that if the a_k's are samples from a random variable with any PDF, then we still get Rayleigh PDF for the amplitude of the received return.[3, pp. 31] When the reflected signal contains a dominant component, as opposed to the case of multiple scatterers where they all contribute equally, in addition to the Rayleigh-distributed RV, it can usually be described by choosing k=2 in equation 2.27, turning it into a chi-square distribution of degree 4. Since the rate of fluctuations is an important factor in radar detection, this rate of change has been divided into two categories:

1. where there are no changes in the amplitude of all the pulses in the train of pulses but that amplitude is a single RV with one of the two PDFs previously mentioned.
2. where the amplitude of each pulse in the train of pulses is a statistically independent RVs with the same PDF.

The first case is called a "scan-to-scan" fluctuating target and the second case is a "pulse-to-pulse" fluctuating target. Therefore, with two possible rates of fluctuations and two PDFs — Rayleigh/exponential and the fourth degree chi-squared distributions — there are four possible combinations amongst fluctuating targets which are known as the Swerling Cases I through IV, extensively studied by Peter Swerling (1929-2000).[3, pp. 32] Suppose, for example, that a target is present at a particular location and consider a radar with a certain beamwidth of θ radians, beaming off an antenna that rotates at a constant angular velocity Ω radians per second and emits at some constant PRF of f_R in hertz. Every time the radar completes a 360° sweep, the target intercepts a new burst of $n = (\theta/\Omega)f_R$ pulses from the main beam. In analogy to the Swerling cases, the "scan-to scan" situation assumes that the set of n echo pulses received back at the radar are all perfectly correlated, in other words, that all n pulses collected in one sweep would have all the same amplitude value. The next set of n pulses collected in the consecutive sweep would also have all the same value as one another, but their value would be independent of the value measured in the first sweep. On the other hand, the "pulse-to-pulse" situation assumes that each individual pulse in each sweep results in an independent value for σ.[28, pp. 80-81] Many modern systems are now designed to transmit bursts of pulses at a constant PRF, with the antenna staring at in a fixed direction.

The time interval required for this measurement is called the coherent processing interval (CPI) and is simply given by n/f_R, which we called illumination time in section 2.1. The Swerling models are simply intended to address the common problem of detection decision making based on not one, but n echo samples. Though first let us address what this common problem is and what detection is all about.

2.3 Radar and Threshold Detection

Since the radar return is always accompanied by noise, the detection circuit is supposed to detect the existence of a target without being confused by this noise. A simple detection circuit consists essentially of a narrow bandpass, or matched, filter, followed by an envelope detector, which typically has a linear or a square law characteristic. The choice of the detector tends to influence the overall performance of the detection and could be dependent on the PDF chosen to describe the interference.[32, pp. 383] The output is fed into a sampling stage. When sampling a signal at discrete intervals, the sampling frequency must be greater than twice the highest frequency of the input signal in order to be able to reconstruct the original perfectly from the sampled version. This minimum sampling frequency is known as the Nyquist frequency and if it were to be smaller than this it would result in signal aliasing — distortion or error due to misidentified signal frequency. The last stage is usually a threshold circuit, in which the output of the envelope detector is compared to a predetermined value known as the threshold. Whenever the envelope surpasses this threshold, the existence of a target is assumed at the corresponding delay. A simple layout of this is schematically illustrated through the block diagram shown in figure 2.8. There are a few choices regarding the detector

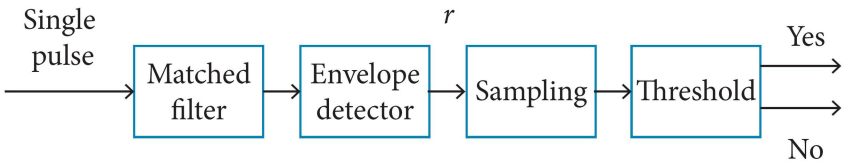

Figure 2.8: Basic receiver setup block diagram with the representation of the main stages of the detection process. The original input is a single-pulse detection and the final output is a boolean decision on declaring the existence of a target, r denotes the linear nature of the envelope detector.

stage. Even though a detector performance analysis is out of the scope of this project, it would suffice to note that it is well established that the Bessel detector has a higher computational cost than the linear detector, which itself has a greater computational cost than the square law detector.[32, pp. 383] Choosing the best detector for a specified application should be first done by understanding the computational cost and performance of said detector.

2.3.1 Single-Pulse Detection

When white Gaussian noise is passed through a narrow bandpass filter, the output noise can be described by the following relation

$$n_0(t) = X(t)\cos(\omega_C t) + Y(t)\sin(\omega_C t) \tag{2.36}$$

where ω_C is the center frequency of the filter. $X(t)$ and $Y(t)$ are two independent random variables (RV) having a Gaussian PDF with a zero mean value and each having the same variance as $n_0(t)$. If the noise spectral power density is $N_0/2$ and the bandpass filter has a rectangular response with the bandwidth f_B, then

$$\overline{X^2(t)} = \overline{Y^2(t)} = \overline{n_0(t)} = N_0 f_B$$

The signal, which is a sine wave of duration τ, at a frequency ω_C, will pass the filter almost unchanged (assuming $f_B \gg 1/\tau$). At the output, during τ, the signal can be described by

$$s_0(t) = A\cos(\omega_C t - \phi_S)$$

or in a canonical form similar to equation 2.36, namely

$$s_0(t) = a\cos(\omega_C t) + b\sin(\omega_C t) \tag{2.37}$$

where

$$A = \sqrt{(a^2 + b^2)}$$

and

$$\phi_s = \arctan\left(\frac{b}{a}\right)$$

The combined signal and noise at the output of the filter will be the sum of 2.36 and 2.37:

$$\begin{aligned} c_0(t) &= s_0(t) + n_0(t) \\ &= [a + X(t)]\cos(\omega_C t) + [b + Y(t)]\sin(\omega_C t) \\ &= r(t)\cos(\omega_C t + \phi(t)) \end{aligned} \tag{2.38}$$

where

$$r(t) = \left([a + X(t)]^2 + [b + Y(t)]^2\right)^{1/2} = \left[X_1^2(t) + Y_1^2(t)\right]^{1/2} \tag{2.39}$$

and

$$\phi(t) = \arctan\left(\frac{b + Y(t)}{a + X(t)}\right) = \arctan\left(\frac{Y_1(t)}{X_1(t)}\right) \tag{2.40}$$

A linear envelope detector will yield the envelope $r(t)$ at its output, where clearly the transformations

$$X_1(t) = a + X(t) \qquad\qquad Y_1(t) = b + Y(t)$$

were applied. As we already discussed, both $X(t)$ and $Y(t)$ are independent Gaussian RV with zero average. Hence, $X_1(t)$ is a Gaussian RV with an average a and $Y_1(t)$ is a Gaussian RV with an average b. Both are independent and can be described by their corresponding PDFs, given by:

$$p_1(X_1) = \frac{1}{\beta(2\pi)^{1/2}}\exp\left(\frac{-(X_1 - a)^2}{2\beta^2}\right) \tag{2.41}$$

and

$$p_2(Y_1) = \frac{1}{\beta(2\pi)^{1/2}}\exp\left(\frac{-(Y_1 - a)^2}{2\beta^2}\right) \tag{2.42}$$

Note that both X_1 and Y_1 have the same standard deviation β, which is also equal to the Root Mean Square (RMS) value of the noise, $n_0(t)$. In other words,

$$\beta = \left(\overline{n_0(t)^2}\right)^{1/2} = \sqrt{N_0 f_B}$$

Given their independence from each other, the two-dimensional joint PDF is equal to the product shown in the following equation 2.43.

$$p(X_1, Y_1) = p_1(X_1)p_2(Y_1) = \frac{1}{2\pi\beta^2} \exp\left(\frac{-(X_1 - a)^2 - (Y_1 - b)^2}{2\beta^2}\right) \tag{2.43}$$

If we perform a simple transformation of X and Y into two other variables r and ϕ, using the following relations:

$$X_1 = r\cos\phi \qquad\qquad Y_1 = r\sin\phi$$

and followed by a Jacobian operation, namely dividing 2.43 by the determinant $|J(X_1, Y_1)|$, this will lead to the transformed joint PDF version of equation 2.43 as a function of te new variables. If we then integrate over all phases, we obtain the envelope PDF of the signal. The solution of the integral is known as the modified Bessel function of order zero, $I_0(x)$ and the result is given by equation 2.44, also known as the Rician probability density function, after Stephen Oswald Rice (1907-1986).

$$p(r) = \frac{r}{\beta^2} \exp\left(\frac{-(r^2 + A^2)}{2\beta^2}\right) I_0\left(\frac{rA}{\beta^2}\right) \tag{2.44}$$

If we happen to assume no signal ($A = 0$) and note that $I_0(0) = 1$, equation 2.44 will yield the PDF of the envelope of the narrow-band noise shown in equation 2.45.

$$p_0(r) = \frac{r}{\beta^2} \exp\left(\frac{-r^2}{2\beta^2}\right) \tag{2.45}$$

which happens to yield the Rayleigh PDF for amplitude, as shown in equations 2.26 and 2.35. Detection, tracking and imaging are the primary functions to be carried out by radar signal processing. Wether a given radar measurement is the result of an echo from a target or simply the effects of interference, further processing is undertaken if the measurement indicates the presence of a target.[28, pp. 295]

2.3.2 Detection, Miss and False Alarm Probabilities

For any radar measurement that is to be tested for the presence of a target, one of two hypothesis can be assumed:

- the measurement is a result of interference only — H_0
- the measurement is a combined result of interference and echoes from a target — H_1

Because the signals are described statistically, the decision between the two hypothesis is an exercise of statistical decision theory. The first hypothesis will be denoted by H_0 and is known

as the null hypothesis while the second hypothesis, known as the alternative hypothesis, will de denoted by H_1. If H_0 happens to best account for the detected data, then the system declares that a target was not present at the range, angle or Doppler coordinates of that measurement. Evidently, if that is not the case then H_1 is declared. Assume that the pre-established threshold happens to be set at a level above all but the highest noise peak, so only one noise peak is mistaken for a target, such as what is shown in figure 2.9. This is called a *false alarm*. Also assume that one of the targets has such a weak signal that it doesn't go over the threshold. This is called a *miss* and means that the probability of detection is less than unity. Clearly, lowering the threshold will increase the probability of detection, but at a cost

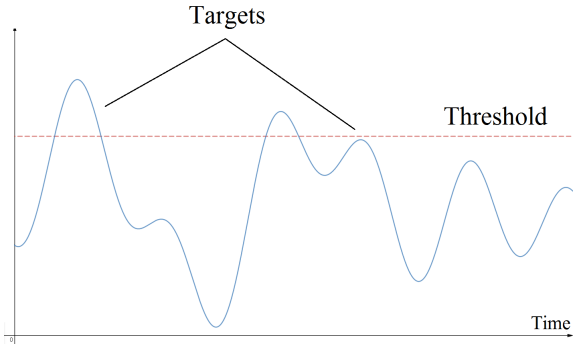

Figure 2.9: Illustration of recognized and unrecognized target peaks amidst noise in a detected signal envelope and stipulated threshold where the YY axis represents relative power units.

of increasing the probability of false alarms. Though, if the SNR were higher, implying higher signal peaks, the smaller target return that wasn't detected before would now have crossed the threshold and the probability of detection would therefore have increased. Thus it has just been demonstrated qualitatively that there's a threefold dependency between signal to noise ratio, probability of detection and probability of false alarm.[3, pp. 37] The quantitative analysis starts with a statistical description of the PDF that describes the measurement to be tested under each of the two hypothesis. If the sample to be tested is denoted by y, then the following two PDFs are required:

1. $p_y(y|H_0)$ = PDF of y given that a target wasn't present.
2. $p_y(y|H_1)$ = PDF of y given that a target was present.

Where 1. is the Rayleigh PDF of equation 2.45 and 2. is the Rician PDF of equation 2.44. Analysis of radar performance is dependent on estimating these PDFs for the system and scenario at hand. Detection will be based on N samples of data y_n forming a column vector $\vec{y}$. The N dimensional joint PDFs $p_y(\vec{y}|H_0)$ and $p_y(\vec{y}|H_1)$ are then used. The following probabilities of interest are defined assuming the two PDFs are successfully modelled:

1. P_D — Probability of Detection: probability that a target is declared (i.e. H_1 is chosen) when a target is in fact present.
2. P_{FA} — Probability of False Alarm: probability that a target is declared (i.e. H_1 is chosen) when a target is not present.

3. P_M — Probability of Miss: probability that a target is not declared (i.e. H_0 is chosen) when a target is actually present.

Since $P_M = 1 - P_D$, the first two are enough to specify all of the probabilities of interest. Since the problem is statistical and as the latter two definitions imply, it is important to realize that there will be a finite probability that the decisions will be wrong.[28, pp. 296-297]
If some threshold level V_T is established, we can impose the assertion that whenever $r > V_T$ the existence of a target is declared. The probability of false alarm is equal to the area underneath the $p_0(r)$ curve (equation 2.45) from the threshold level to infinity while the probability of detection is equal to the area underneath $p(r)$ curve (equation 2.44), also from the threshold level to infinity. This is:

$$P_{FA} = \int_{V_T}^{\infty} p_0(r)\, dr = \exp\left(\frac{-V_T^2}{2\beta^2}\right) \tag{2.46}$$

and

$$P_D = \int_{V_T}^{\infty} p(r)\, dr = \text{tabulated solution} \tag{2.47}$$

Even though the integral of equation 2.47 can only be expressed by a tabulated function, a simplifying approximation can be made for large SNRs, i.e. when

$$\text{SNR} = \frac{P_R}{N} = \frac{A^2}{2\beta^2} \gg 1$$

If this condition is met, there is then an approximation that can be made to the modified Bessel function

$$I_0(x) \approx \frac{1}{\sqrt{2\pi x}}\, e^x$$

that will finally lead to a Gaussian shaped PDF given by:

$$p(r) \approx \frac{1}{\sqrt{2\pi}\beta}\, \exp\left(\frac{-(r+A)^2}{2\beta^2}\right) \tag{2.48}$$

Since the integral of a Gaussian PDF is very well known, a close approximation of the value of P_D can be calculated under these circumstances.

$$P_D = p(V_T < r < \infty) \approx \frac{1}{2}\left[1 - \text{erf}\left(\frac{V_T}{\beta\sqrt{2}} - \sqrt{SNR}\right)\right] \tag{2.49}$$

We have now quantitatively proven that P_{FA}, P_D and SNR indeed have the threefold relationship afore mentioned. Given the dependence of the first probability on the threshold level and of the second probability on the SNR and threshold level, the relation can be summed up in a fairly accurate manner by an empirical expression suggested by Walter J. Albersheim (1897-1982).[3, pp. 42-43] But it is first necessary to introduce the concept of integration in radar detection and its most common application techniques.

2.4 Integration

Thus far, it is clear that the ability to detect targets is inhibited by the presence of noise and clutter. Both can be modelled as random processes. The noise as uncorrelated from sample to sample, and clutter as partially correlated from sample to sample. Target detection will be easy when a single target is placed in the line of sight of the radar with no clutter at all. But practical targets appear in clutter with multiple reflected echoes from multiple sources. Though it is out of the scope of this document, many researchers developed various detection techniques as a solution to this problem.[31, pp. 141] As for the target, we already know that it can be modelled as either nonfluctuating — a constant — or a random process that can be completely correlated, partially correlated, or uncorrelated from sample to sample — the Swerling cases. Since a target may be in view for several consecutive pulses, it's usually beneficial to decide on the existence of a target on the basis of more than one pulse. The signal-to-interference ratio and thus the detection performance are often improved by integrating — adding — multiple samples of the target and interference, motivated by the idea that the interference can be "averaged out" when summing multiple samples.[28, pp. 322] Simply put, pulse integration is an improvement technique conceived to address gains in the detection capability by using multiple transmit pulses. Figure 2.10 illustrates the difference between a pair of coherent and noncoherent pulses in terms of their phase shift or lack there of. Data

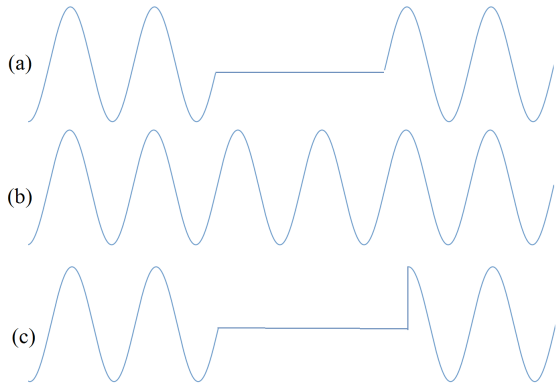

Figure 2.10: Qualitative concept illustration of a (a) coherent and (c) noncoherent pair of pulses, generated off the same (b) reference sinusoid.

can be integrated at three different stages in the processing chain:

1. After demodulation, to the complex-valued magnitude and phase (Q and I) data. Combining complex data samples is referred to as *coherent integration*.
2. After envelope detection, to the signal's magnitude data. Combining magnitude samples after the phase information is discarded is referred to as *noncoherent integration*.
3. After threshold detection, to the target present/absent decisions. This technique is called *binary integration* and will not be further developed.

A system could elect to use none, one or any combination of these techniques. The major cost of integration is the time and energy required to obtain multiple samples of the same range and/or angle cell (or multiple threshold detection decisions for that same cell). This is time that can't be spent searching for targets elsewhere, updating already known targets or even imaging other regions of interest. Integration also increases the signal processing computational load.[28, pp. 323]

2.4.1 Coherent Integration

Coherent integration can be performed if the target reflects each pulse with a non-random initial phase and the propagation medium does not randomize the phase. It is also necessary to know the initial phase of each transmitted pulse. An interrupted continuous-wave (CW) signal, such as the ones shown in figures 2.2 and 2.10 (a) are a form of coherent pulses. Coherent pulses are processed in the receiver in an optimal way, yielding the highest improvement in SNR out of all the techniques.[3, pp. 44-45] To perform coherent integration, a synchronous

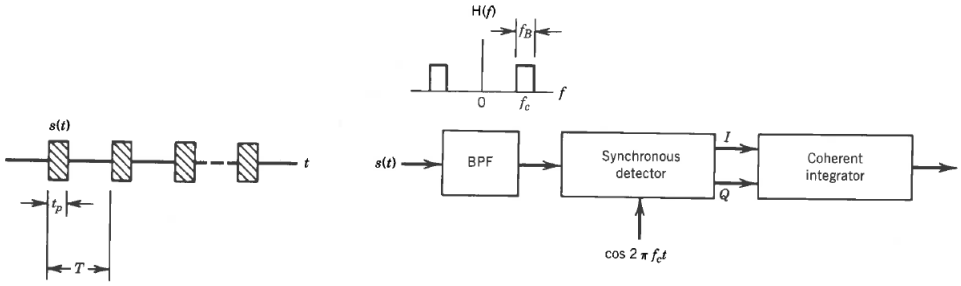

Figure 2.11: Block Diagram of a coherent integration receiver setup. The graph on the left represents input pulse train signal being fed into the receiver.

detector and signal processor must be present. The synchronous, or coherent, detector retains phase information through the in-phase (I) and quadrature (Q) components allowing for a coherent integration. After it accumulates the n pulse sum, the signal processor performs the envelope detection, sampling and threshold check. Coherent processing can be viewed as joining the pulses together into a single longer pulse with linear phase build up ($\phi = \omega t$).[3, pp. 45] Thus n pulses, each with duration t_P can be viewed as a single-pulse of duration nt_P. A rectangular filter necessary to pass one pulse of duration t_P without adding unnecessary noise has the bandwidth $f_B = 1/t_P$ which will ideally yield a noise power at its output of

$$N_1 = N_0 f_B = \frac{N_0}{t_P} \tag{2.50}$$

where $N_0 = N_F k_B T$ is the noise spectral power density in W/Hz as seen in equation 2.12 of section 2.1 and the subscript 1 indicates we are dealing with one pulse. The noise power at the output of a rectangular filter matched to a pulse of duration nt_P — done by decreasing the bandwidth to f_B/n — is:

$$N_n = \frac{N_0}{nt_P} = \frac{N_1}{n} \tag{2.51}$$

Thus we see that the output noise power has been lowered by a factor of n. On the other hand, the signal power at the output will reach its input level after a rise time equal to the inverse of the bandwidth (i.e., to t_P in the case of a single-pulse and to nt_P in the case of the integrated pulse of duration nt_P). The conclusion is that at the end of the integration period, the signal power will be the same for one pulse or for n pulses integrated coherently, but the noise power in the n-pulses case will be n times lower. Hence there will be an improvement of n SNR. Simply put, the processing concept consists of combining the n pulses into a single-pulse n times as long and passing it through a filter n times as narrow. This is only one of the many possible methods of coherent integration though the result will always be the same no matter what the method is — an improvement of n in the SNR.
The restriction of having to know the initial phase of each transmitted pulse (for reference when processing the received signal), as well as the requirement for retaining coherency during the propagation and reflection of the signals might be too severe for many applications. This often leads to a rather less optimal processing called *noncoherent integration*.[3, pp. 45]

2.4.2 Noncoherent Integration

In noncoherent integration, phase information is discarded and instead, is performed *after* the envelope detector, where the magnitude, or square magnitude in the case of a square-law detector, of the data samples is integrated. Most classical detection results have been developed for the square-law detector. A conceptual block diagram for a noncoherent integration receiver is shown in figure 2.12. The receiver consists of a filter matched to the

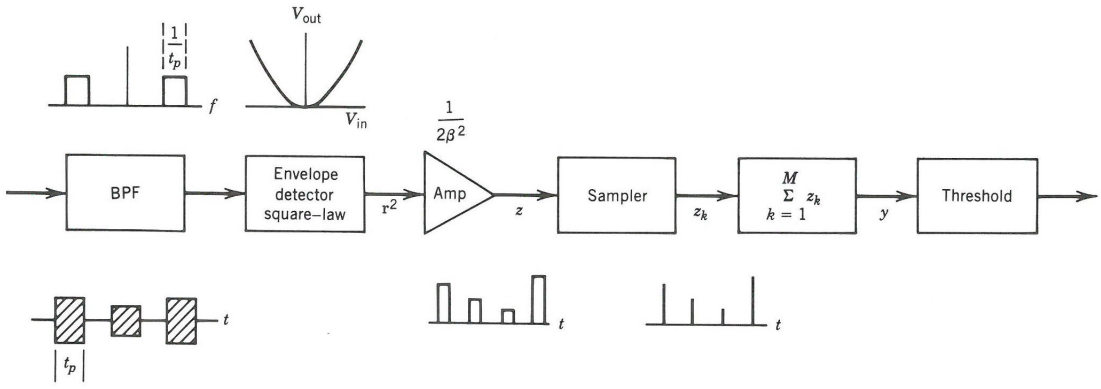

Figure 2.12: Block Diagram of a receiver setup meant for noncoherent integration. The graphs above and under the BPF block represent the filter's bandwidth and the signal's pulsewidth, respectively. The r^2 term and the voltage graph above the envelope detector block denote the squared nature of the detector. z denotes the amplified version of the signal and z_k the individual samples taken from z at a given sampling frequency. M in the summing block represents the number of pulses used for integration, up to now denoted by n.

width of a single-pulse, an envelope detector with a square-law characteristics, a sampler that takes one sample of the envelope detector per pulse (all equally delayed from their respective

transmitted pulses), an adder that sums n of these samples and a threshold stage to finish. Even though a square-law detector was selected for the diagram, in practice there is very little difference in integration performance between a linear detector and a square-law detector.[3, pp. 45-47]
Noncoherent integration is implemented by summing n samples from n pulses. Assuming a pulse repetition period much longer than the pulse duration t_P and noting that the noise was passed through a filter with $1/t_P$ bandwidth, we can conclude that the additive noise samples, taken at the pulse repetition intervals, are uncorrelated. Thus, the envelope of the received pulses are uncorrelated random variables, with a PDF given by equation 2.44. With a further change of variables that allow the envelope samples to be normalized to the RMS value of the noise, β, a relationship stating that the required SNR_P decreases with the inverse of $\sqrt{n}$ can be reached.[3, pp. 49]

Albersheim's Equation

The performance results for the case of a nonfluctuating target in complex Gaussian noise are given by two difficult integrals that determine P_{FA} and P_D. While it might be undemanding to implement in a powerful numerical computing environment such as MATLAB™ and similar software analysis tools, these equations are not easy to manually calculate. Fortunately, a simple closed-form expression that can be easily computed, relating P_{FA}, P_D and SNR_P, exists. The expression is know as *Albersheim's equation* and despite its simplicity, this empirical equation is remarkably accurate. It applies under the following conditions:

- Nonfluctuating target in Gaussian noise.
- Linear, instead of a square-law, detector.
- Noncoherent integration of n samples.

Albersheim's equation is an empirical approximation to the 1967 results by Robertson for computing single-sample SNR required to achieve a given P_D and P_{FA}.[28, pp. 329] The estimation is given by a series of calculations of the following nature:

$$\begin{aligned} \text{SNR}_{P(dB)} &= -5 \cdot \log_{10}(n) + \left[6.2 + \left(\frac{4.54}{\sqrt{n+0.44}}\right)\right] \cdot \log_{10}(A + 0.12AB + 1.7B) \\ A &= \ln\left(\frac{0.62}{P_{FA}}\right) \\ B &= \ln\left(\frac{P_D}{1-P_D}\right) \end{aligned} \tag{2.52}$$

Note that the single sample Signal-to-Noise Ratio is in decibels, hence the notation $SNR_{P(dB)}$, and it should be emphasize that equation 2.52 represents the SNR at the output of a bandpass filter matched to a single pulse.[3, pp. 49]. The error in the estimate of $SNR_{P(dB)}$ through this relationship is less than 0.2 dB for a very useful range of parameters. Namely,

$$10^{-7} \leq P_{FA} \leq 10^{-3} \qquad 0.1 \leq P_D \leq 0.9 \qquad 1 \leq n \leq 8096$$

For the special case of $n = 1$, equation 2.52 reduces to its simplest version:

$$\begin{aligned} \text{SNR}_{P(dB)} &= 10 \cdot \log_{10}(A + 0.12AB + 1.7B) \\ A &= \ln\left(\frac{0.62}{P_{FA}}\right) \\ B &= \ln\left(\frac{P_D}{1 - P_D}\right) \end{aligned} \tag{2.53}$$

The mutual dependency between the three quantities has proven to be accurately expressed through Albersheim's equation and is illustrated in figure 2.13 for a single sample through equation 2.53. One can notice that for the same probability of detection, for a decrease in the

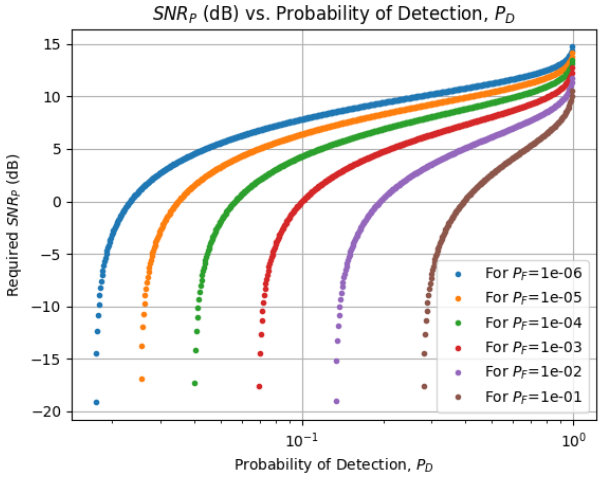

Figure 2.13: Quantitative illustration of the threefold dependency of P_D, P_{FA} and SNR_P. For a fixed P_D close to 1, a decrease in the P_{FA} clearly leads to an increase in the required single-pulse SNR.

probability of false alarm (i.e. as it approaches zero) the minimum required single-pulse SNR increases. Suppose $P_D = 0.9$ and $P_{FA} = 10^{-6}$ are required in a system under the previous conditions and the detection is to be based on a single pulse. The required SNR of that sample is a direct application of Albersheim's equation 2.53 and the result yields $\text{SNR}_P = 13.14$ dB. If $n = 100$ samples are noncoherently integrated, it should be possible to obtain the same P_D and P_{FA} with a lower single-pulse SNR. To have this confirmed, we can use equation 2.52: A and B remain unchanged but the required SNR_P is now reduced to -1.26 dB. In this case, the noncoherent integration gain of $G_{nc(dB)} = 13.14 - (-1.26) = 14.4$ dB is much better than the $\sqrt{n}$ rule of thumb usually given for noncoherent integration.[28, pp. 330] Equations 2.52 and 2.53 therefore provide solid means for the calculation of the required SNR_P given P_D, P_{FA} and n. It is possible, however, to solve 2.52 for either P_D or P_{FA} in terms of the other as well as SNR_P nut not in terms of n. Solving Albersheim's equation for n in a standard manner seems to be impossible since it appears both in logarithmic and square-root form. Though there is an approximation that can be made to achieve a very close result.[33, pp. 2-3] The following relations in 2.54 show how to estimate P_D given the other factors, where SNR_P is in dB. The resulting relation between P_D, P_{FA} and SNR_P can be best represented by the so called receiver

operating characteristics (ROC) curve, plotted in figure 2.14.[33, pp. 1-2]

$$
\begin{aligned}
A &= \ln\left(\frac{0.62}{P_{FA}}\right) \\
Z &= \left(\frac{\text{SNR}_{P(dB)} + 5 \cdot \log_{10}(n)}{6.2 + \frac{4.54}{\sqrt{n+0.44}}}\right) \\
B &= \ln\left(\frac{10^{Z} - A}{1.7 + 0.12A}\right) \\
P_D &= \frac{1}{1 - e^{-B}}
\end{aligned}
\tag{2.54}
$$

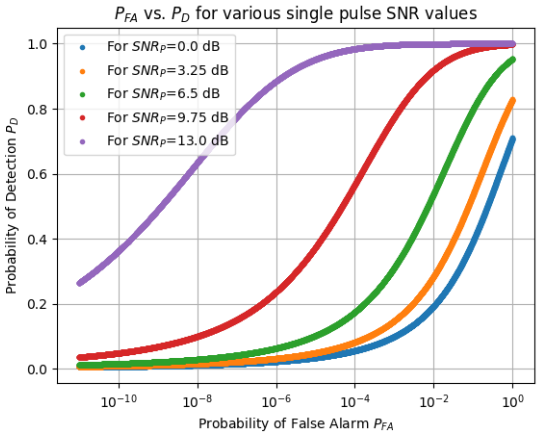

Figure 2.14: The Receiver Operating Characteristics (ROC) curve is the one that best illustrates the threefold dependency of P_D, P_{FA} and SNR_P. Low SNR signals clearly can't guarantee acceptable probabilities without compromising the rate of false alarms.

Noncoherent Gain

The noncoherent integration gain, G_{nc}, mentioned at the end of section 2.4.2, is the reduction in single-sample SNR required to achieve a specified P_D and P_{FA} when n samples are combined. In decibels, this is given by equation 2.55.

$$
\begin{aligned}
G_{nc(dB)}(n) \quad &= \text{SNR}_{P(dB)}|_{1\ pulse} - \text{SNR}_{P(dB)}|_{n\ pulses} \\
&= 5 \cdot \log_{10}(n) + \left[6.2 + \left(\frac{4.54}{\sqrt{n+0.44}}\right)\right] \cdot \log_{10}(A + 0.12AB + 1.7B) \\
&\quad + 10 \cdot \log_{10}(A + 0.12AB + 1.7B) \\
&= 5 \cdot \log_{10}(n) - \left[\left(\frac{4.54}{\sqrt{n+0.44}}\right) - 3.8\right] \cdot \log_{10}(A + 0.12AB + 1.7B)
\end{aligned}
\tag{2.55}
$$

While on a linear scale, the noncoherent gain can be given by the following simplified equation:

$$
G_{nc}(n) = \frac{\sqrt{n}}{k^{f(n)}} \tag{2.56}
$$

where

$$\begin{aligned} k &= A + 0.12AB + 1.7B \\ f(n) &= \left(\frac{4.54}{\sqrt{n + 0.44}} \right) - 3.8 \end{aligned} \tag{2.57}$$

The constant k possesses the terms that are not dependent of n, while the term $f(n)$ is a slowly declining function of n.[28, pp. 331]

The evolution of $G_{nc(dB)}(n)$ from equation 2.55 versus the number of noncoherent integrated

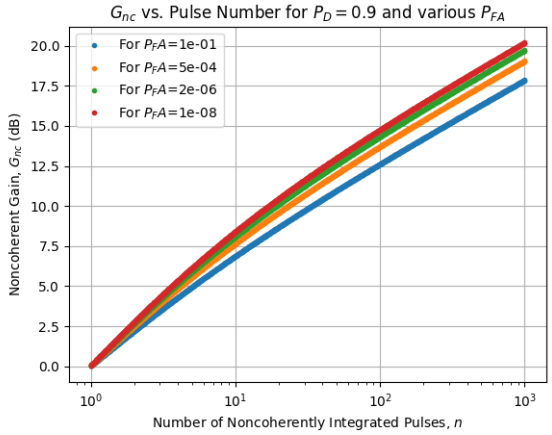

Figure 2.15: Noncoherent gain behaviour as a function of the number of noncoherently integrated pulses n used for a detection probability of $P_D = 0.9$ and various false alarm probabilities. For a fixed n, as the false alarm probability increases to approache 1, the noncoherent gain, $G_{nc}(n)$ increases.

pulses is plotted in figure 2.15. Noticeably, if a number of pulses n is fixed, a decrease in the probability of false alarm (i.e. as it approaches zero) also leads to a decrease in the noncoherent gain. The gain eventually slows in an almost asymptotical manner to eventually become proportional to $\sqrt{n}$ for large n and so the XX axis was plotted in a logarithmic scale to better distinguish each curve's behaviour near the origin. Therefore the noncoherent gain is more efficient than the $\sqrt{n}$ often attributed to this kind of integration for a wide range of n but remains less efficient than coherent integration since it doesn't achieve a full gain of $n\text{SNR}_P$. Nevertheless, by not requiring phase information, its much simpler implementation means it's widely used to improve the SNR before the threshold detector stage.

Having now concluded an analysis on the theory behind some of the most important radar principles, it is time to apply these concepts into projecting the performance of the Flores radar introduced in section 1.3.

Chapter 3

Radar Options Specifications

3.1 Gain

Since no gain value was yet established for the SST radar in question a small calculation would lend itself useful to determine the variation in gain from the HAX radar assuming the electronics components that determine its efficiency remain equal. As was seen in section 2.1, equation 2.10, the effective area of an antenna, $A_e = A_T$, is directly related to its geometrical area, A_{geo} and to the gain. The effective to geometrical antenna area ratio of the HAX radar is close to 51%.

$$\frac{A_e}{A_{geo}} = \frac{\lambda^2 G}{4\pi A_{geo}} = \varepsilon \approx 0.51$$

Using that same figure to calculate the Flores antenna's effective area with equation 2.10 and then its gain through equation 2.9, the determined gain is shown in table 3.1. For a 1 meter increase in the antenna's diameter to 13.2 m as compared to the HAX's 12.2 m antenna, the gain becomes 64.32 dB as opposed to 63.64 dB.

Antenna Properties	**HAX**	**Flores SST**
Diameter, D	12.2 m	13.2 m
Gain, G	63.64 dB	64.32 dB

Table 3.1: Diameter and Gain differences between the considered antennas assuming an equal efficiency factor for both radars.

3.2 Noise Figure

Even though the conditions for the simulation are ideal and so is the virtual equipment, a noise figure as defined in section 2.1 could be set as 0 dB since we are not dealing with a practical receiver. Though, in an attempt to mimic some of the real known parameters, the simulation of the Flores radar performance was done also with the HAX's system temperature of $T_e = 161$ K which, when taken as the noise, or effective, temperature of the system, will

result in a close approximation of the system's noise figure, N_F. Which is the noise factor — ratio of the output to the input noise power — but in dB. Taking the standardized room temperature as $T_{amb} = 290$ K, a simple calculation led to a feasible value.[34]

$$T_e = (10^{\frac{N_F}{10}} - 1) \cdot T_{amb}$$

$$N_F = 10 \cdot \log_{10}(1 + \frac{T_e}{T_{amb}}) = 1.918 \text{ dB}$$

3.3 Requirements

Let us first recall that the two stipulated requirements for a space debris tracking radar are the following:

1. SNR_P from a 0 dBsm target (1 m^2) at R = 10^3 km should be greater than 41 dB
2. R of a SNR_P = 3 dB from a -40 dBsm target (1 cm^2) should be detected at 900 km

In other words, the nominal sensitivity which is determined by single-pulse SNR from a 0 dBsm (1 m^2) target at a distance of 1000 km should be greater than 41 dB. And the detection of a 3 dB single-pulse SNR from a -40 dBsm (1 cm^2) target at 900 km should be accomplished. With the newly determined parameters of gain and noise figure, we can input all the required parameters values into equation 2.15 and simulate the radars response to certain range, SNR and RCS conditions. Figures 3.1 (a) and 3.2 (a) each show, in the blue coloured plots, that the parameters planned for the antenna at Flores Island do meet the first and second SST stipulated requirements.
Since a future Azorean radar is being analysed, a second option that was also considered was the 32-meter antenna built in the island of S. Miguel at a similar latitude (37.7º). For comparison reasons, the performance of a more powerful setup is shown beside the Flores' radar performance in figures 3.1 (b) and 3.2 (b). Specifically, a bistatic configuration between the S. Miguel antenna operating in the X-band around 10 GHz and the American Goldstone antenna as a transmitter station was declared and their distinct diameters and gains are shown in table 3.2. This could also be done with emitter stations at TIRA (Germany) or Evpatoria (Ukraine).

Antenna Properties	**S. Miguel**	**Goldstone**
Diameter, D	32 m	70 m
Gain, G	66.0 dB	74.4 dB

Table 3.2: Main features of the considered antennas for bistatic configuration.

3.4 System Loss

Since the actual loss causes and estimates are out of the scope of this project, it is one of the few parameters that can be willingly varied to fit operational needs. A system loss

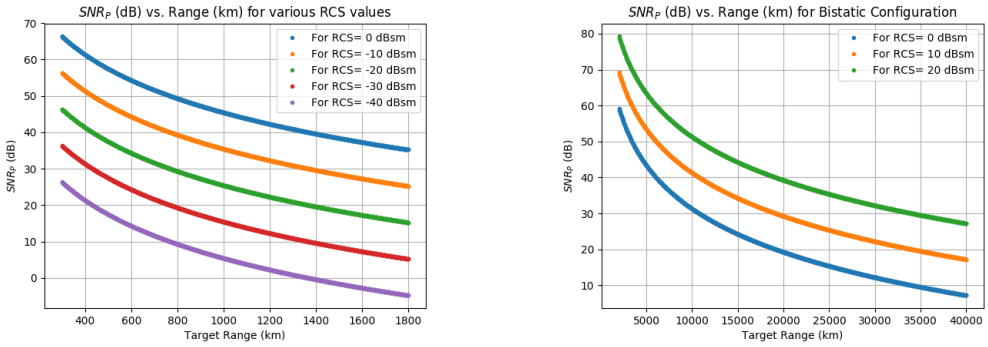

(a) Monostatic (b) Bistatic

Figure 3.1: Signal-to-Noise ratio in dB versus target range in kilometers for multiple target radar cross sections from 1 m^2 (0 dBsm) to 1 cm^2 (-40 dBsm). A system loss factor of 1 dB leads to 45.4 dB return SNR_P at 1000 km for a 0 dBsm target (1 m^2). We can then adjust and affirm that an additional 4.4 dB system loss can be supported in order to meet the first requisition, yielding a return SNR of 41.03 dB in that case. The bistatic performance in (b) shows suitable detection capabilities up to GEO for large debris objects which can be further increased with integration techniques.

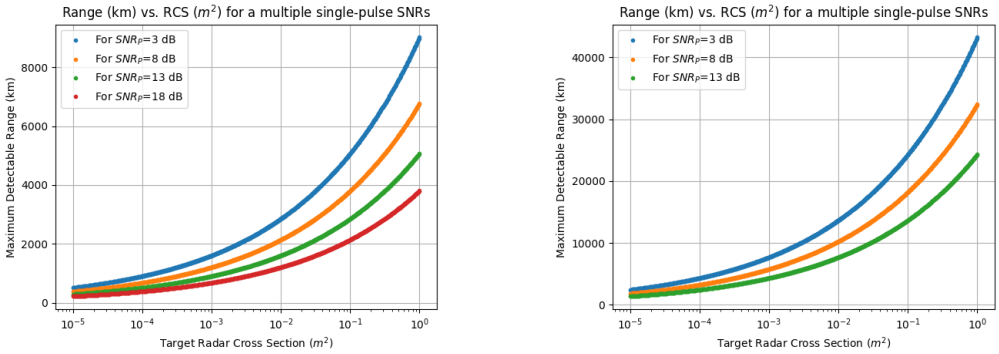

(a) Monostatic (b) Bistatic

Figure 3.2: Target range in kilometers versus target radar cross section in m^2. A 3 dB SNR_P from a -40 dBsm (1 cm^2) target that should at least be detected at a 900 km range is in fact detectable at just under 1150 km instead when a system loss factor of 1 dB declared. We can still admit an additional 4.2 dB system loss to produce a 903 km range detection, in order to meet and slightly surpass the system's second requirement. The behaviour in (b) is equal but for a broader detection range.

factor of about L= 1 dB was often chosen for the upcoming simulations since many of the real world loss causes are not present in the simulations, such as propagation attenuation or uneven distribution of power in the beam. Since this value successfully helped meet the requirements, loss values that would just make it over the specifications were also determined and are shown in table 3.3 If the system loss starts to go over 4 dB then the requirements cease

System Loss Factor	Requirement 1.	Requirement 2.
L = 1 dB	SNR_P = 45.4 dB	R = 1150 km
L = 4 dB	SNR_P = 41.5 dB	R = 910 km

Table 3.3: Quantitative differences between the nominal sensitivity and range values of the Flores radar for an ideal (1 dB) and a more realistic (4 dB) system loss factor values while still meeting the stipulated requirements.

to be met. We should then resort to a pulse integration technique to increase the detected SNR.

3.5 Pulses and Integration

As was already discussed in the previous chapter, improving the radar's sensitivity through integration will have a significant impact on its capability of debris size detection. In case it was not already noticed, the HAX radar uses 16 noncoherently integrated pulses for detection.[6] For comparison reasons, this value was applied under the Flores SST parameters and an improvement of about 9.5 dB (+18% of its single pulse value) in the SNR is obtained when still considering a 1 m^2 target at 10^3 km. We also saw in section 2.4.2 that, when using 100 samples, a noncoherent gain of 14.4 dB is obtained. A further increase in the number of pulses by the same factor does not produce the same improvement ratio as can be verified in figure 3.3. We saw in subsection 2.4.2 that, to meet the desired probability of detection, $P_D = 0.9$, and probability of false alarme, $P_{FA} = 10^{-6}$, the return SNR_P must be at least 13.14 dB. Since this is a relatively high requirement and might not be very practical, we can make the system more feasible by using the noncoherent pulse integration technique in order do reduce the required SNR. A 16-pulse receiver operating characteristics (ROC) curve is shown in figure 3.4 and we can see how the required SNR has now reduced to about 3.75 dB while maintaining the desired P_D and P_{FA}.

3.6 Simplified System Simulation

A monostatic pulse radar system design was developed with the aid of the Phased Array System Toolbox from MATLAB^{TM} 2016b as an attempt to reproduce close to idealized results in simplified conditions such as the absence of clutter, isotropic radiation patterns and a free space environment. Since the radar system proposed so far is a monostatic, the transmitter and the receiver of the simulation were setup together. The transmitter then generates a pulse that hits a pre-positioned target and produces an echo scatter intercepted

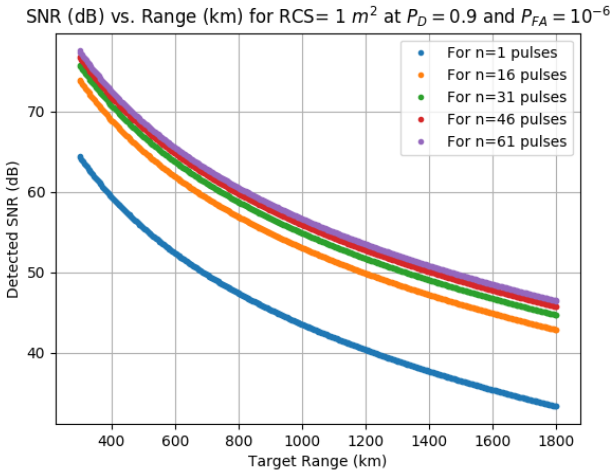

Figure 3.3: Signal-to-Noise ratio versus target range from a 0 dBsm (1 m^2) target for various numbers of noncoherently integrated pulses used for detection. Compared to the single pulse case (n=1), a 15 pulse increase leads to a 9.5 dB increase in the SNR while another 15 pulse increase only yields a further 1.8 dB increase.

back at the receiver. By measuring the location of the echoes in time, the target range can be successfully estimated with an error value contained in the declared range resolution. The system configuration that follows is supposed to simulate an ideal signal return given a radar system's performance in range detection.[35] The desired performance rests on a probability of detection $P_D = 0.9$ and a false alarm probability equal to $P_{FA} = 10^{-6}$. These will be used to determine the minimum required SNR_P and system's detection threshold. Since, as we know, coherent detection requires phase information, a noncoherent detection approach was preferred over the coherent one as to decrease computational demand. To simplify the design, a stationary isotropic antenna was defined as well as 3 nonfluctuating targets each with a RCS between 1 cm^2 and 1 m^2 at a distance of up to 2000 km. In signal processing, white noise is a random signal having equal intensity at different frequencies providing it with a constant power spectral density. The simplest example of white noise is a set of samples that are independent and have identical distribution probability[1]. If the samples happen to have a normal distribution and a mean value of zero, the signal is said to be white Gaussian noise. We know for a fact that the reflected signal will be an attenuated and possibly phase-shifted version of the original transmitted signal with added white noise, though we choose to discard the phase information by later opting for noncoherent detection. So when the output of the matched filter exceeds the given threshold it can be said, with a high degree of certainty, that the signal indeed reflected off the target. By using the pulse's propagation speed and the first instance at which the reflected signal is detected, the object's range is easily estimated. Figures 3.5 show the received echo before and after the matched filter stage is inserted in the processing chain and the SNR_P has noticeably improved. However, even though farther targets were declared with greater RCSs, since the received signal power is dependent on the

[1]Otherwise known as independently and identically distributed (i.i.d.) random variables.

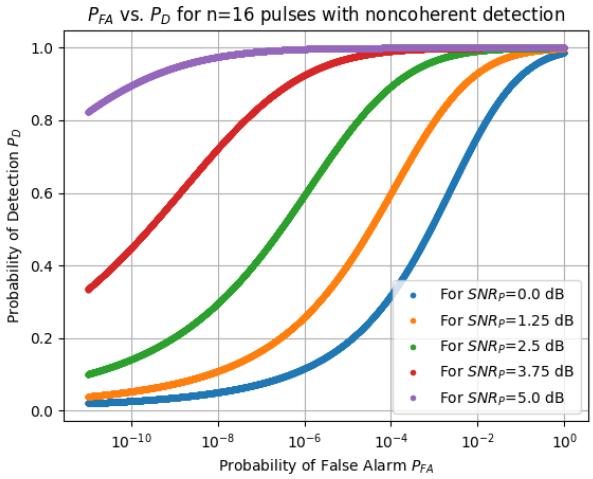

Figure 3.4: Receiver Operating Characteristics (ROC) for $n = 16$ pulses used for noncoherent integration. When compared to the ROC of figure 2.14 a significant improvement is apparent in the lower required SNR_P values needed for the same P_D and P_{FA}.

target's range, the return of a closer target is still much stronger than the return of a target that is farther away. In fact, if the radar range equation 2.15 is recalled, the return is inversely proportional do the fourth power of the target's distance. This can be verified in both graphs of figure 3.5, where the amplitude peaks are successively weaker even though their RCSs were declared successively larger. In terms of the simulation, the noise from a closer range bin also has a significant chance of surpassing the threshold and possibly shadowing a target farther away. To ensure that the threshold treats all targets within the radar's detectable range equally, a time varying gain function can be applied to compensate for the range dependent loss in the received echoes. The application of the time varying gain translates in an incline in the noise floor to ensure the threshold is impartial to all targets. However, the target return is now range-independent, just as intended. A constant threshold can continue now to be used for detection across the entire detectable range. In the case of this simulation, it was around 2000 km, enough to cover the desired space environment. Though, notice in figure 3.6

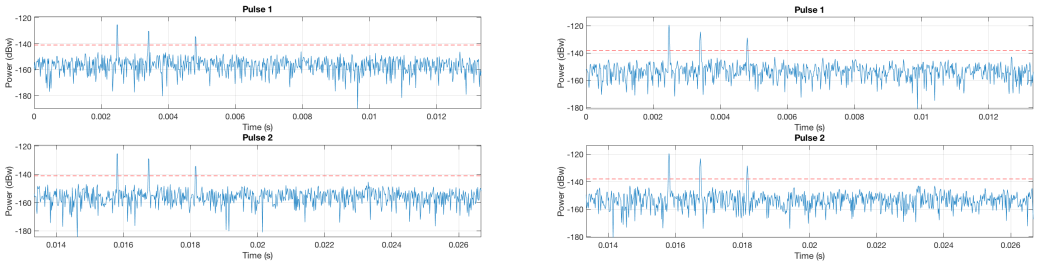

(a) Original untreated echoes

(b) Echoes after matched filter stage

Figure 3.5: Comparison of the received echoes for 2 pulses before and after a matched filter is introduced in the receiver's layout/setup.

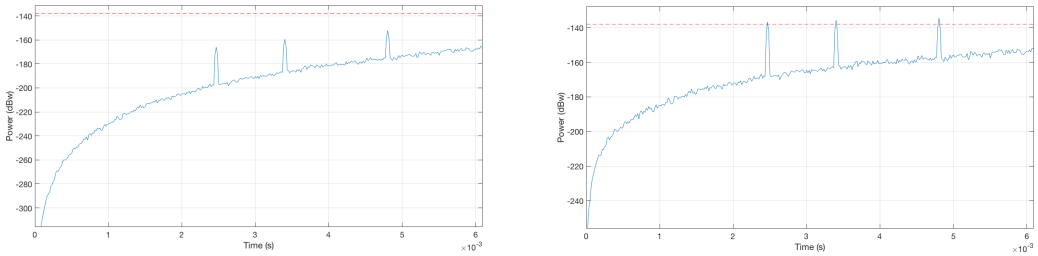

(a) With added time varying gain (b) After noncoherent integration

Figure 3.6: Comparison between the effects of applying noncoherent integration.

(a) that after this step, the threshold is above the maximum power level contained in each pulse and it is clear that nothing can be yet detected at this stage. We need to perform a pulse integration technique to ensure the power of returned echoes from the targets can once again surpass the designated threshold while leaving the noise floor below it. Just as was seen in subsection 2.4.2, we can further improve the SNR by noncoherently integrating the received pulses. After the integration stage, the data is ready for the final detection decision stage. It can be seen from the figure 3.6 (b) that all three echoes from the targets are above the threshold, and therefore can be detected. The detection scheme identifies the peaks and then translates their positions into estimated ranges of the targets. Even though the estimates come very close to the true coordinates, the resulting range estimates are only accurate up to the established range resolution that can be achieved by the radar system.
In a nutshell, the previous simulation procedure can be described by figure 3.7.

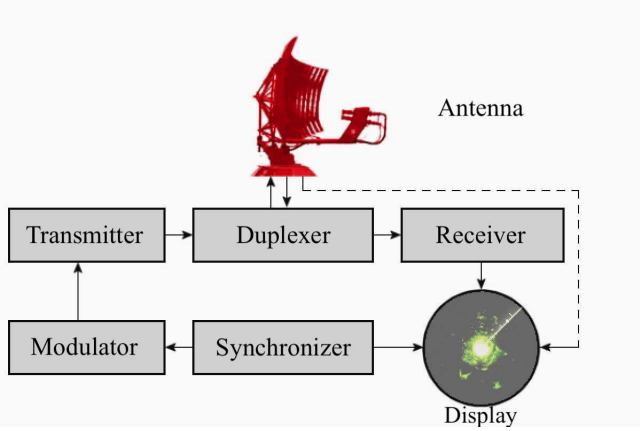

Figure 3.7: Block diagram of the simplified monostatic pulse radar simulation. Adapted from [4]

- The *Synchronizer* supplies the so-called synchronizing signals, such as the duration of the transmitted pulses, the start of the deflection in the indicator, and the timing of other associated circuits.
- The *Modulator* generates the shape $A(t)$ of the transmission signal. In the simplest case, this is only an On/Off switching for the transmitter.

- The radar *Transmitter* produces short duration high radio frequency pulses of energy that are radiated into space in the desired direction by the antenna.
- The *Duplexer* alternately switches the antenna between transmission and reception so that the antenna operates in only one of them given the monostatic nature of the simulation. The high powered pulses off the transmitter would quickly fry the receiver if they were to operate simultaneously.
- The *Antenna* sends out the transmitter energy in the desired direction with its respective distribution and efficiency. The process is applied in a similar manner for reception.
- The *Receiver* filters, amplifies, demodulates and declares or not the existence of a target from the received signals as was already discussed in the previous chapters.
- The *Display*, or Indicator, should present the observer with a continuous and intelligible graphic picture of the target's relative position. This stage was not simulated.

The space catalogue maintenance would then be done in the following manner. The space survey made by the radar would provide several measurements for various objects. A tracking procedure identifies the measurements belonging or not to the same object. Finally, the catalogue correlation procedure either recognizes that the target is already catalogued and updates its orbital parameters, adds new objects — resulting from launches or explosions — or deletes objects — resulting from re-entry or first object explosion. All tracks are correlated to the catalog, they either match and update or they don't and are declared an Uncorrelated Target (UCT).[16, pp. 19] Generally, the criteria to determine track status is associated with the comparison of the estimated position of the debris object with those already present in the catalog. Correlation occurs if the object is within an already stipulated volume. This volume is a 3-dimensional hypothetical box centered on the predicted position and is used to associate tracks of known objects.
Even though this simple simulation illustrates the concept of radar detection, the performance of orbital parameter catalogue maintenance is extremely difficult to demonstrate. Not only would it be necessary to simulate a great deal of the possible measurements, but data processing and correlation would also be required.[12, pp. 34] The effort would essentially consist in producing an actual catalogue and is out of the scope of this document.

Chapter 4

Conclusions and Future Work

Given the limited radar detection coverage of medium to low sized objects and the limited search capability of radars to find and track such objects, constricting the radar's search space is critical to their detection. Clearly, information on the orbital debris environment is crucially needed to determine the current and future hazards that orbital debris poses to space operations since the orbital environment is dynamic and in constant change. Unfortunately, this environment is difficult to accurately characterize since only the largest of debris can be repeatedly tracked by ground-based sensors.

Based on the brief analysis conducted in this document and the estimated parameters for the radar soon to be installed at Flores Island, this radar would have the capability to provide detection and tracking data of medium to low sized debris (under 10 cm) and constructively contribute to SST catalog maintenance. Just like the well-known Haystack and HAX radars, the Flores radar offers the required operational frequency and nominal sensitivity to detect and validate small debris orbit predictions. Also, with sufficient track time, optimal waveform and pulse integration, the Flores radar will easily be able to provide accurate range measurements to meet the necessary criteria. Its performance was determined in order to meet and surpass the essential stipulated requirements for the kind of targets meant to be tracked. With an expected gain of 64.3 dB and noise figure of 1.92 dB, the Flores antenna has all the necessary criteria to belong to a network of space surveying and orbital debris tracking. If a pulse integration technique is applied, such as the noncoherent one often exemplified throughout the document, the required SNR for an accurate detection reduces drastically and virtually the whole LEO can be successfully scanned. The performance of a 32 meter antenna in a bistatic configuration under the similar conditions was briefly studied for comparative effects in order to illustrate the necessary conditions to accurately detect debris on GEO. The larger the antenna's diameter and gain, a greater detection capability quickly follows. More than 60 years into the space age, the implementation of *End-of-Life* options has finally begun for the spacecraft and instruments we propel into orbit. ESA's Clean Space Initiative is worth a mention as it is currently exploring ways of cleaning up our orbital environment as well as pioneering an eco-friendly approach to present and future space activities, preventing the steady build-up of space junk that has been taking place over these decades.[8, 36]

Based upon progress within the SSA program during the 2009–16 period, some of the main

areas that are expected to continue to be in the focus of the SST segment for 2017–20 include a further development of SST networking technologies as well as simulations of the performance of SST architectures and the development of data exchange standards.[17]. There are many ways in which this thesis can evolve into a more detailed document on the development of a ground-based radar for space debris detection as well as the current efforts of mitigation and remediation. An analysis of the Swerling Models for fluctuating targets would be interesting. For instance, in the case of the section 3.6 simulation, if one wanted to estimate the target's speed as it travelled in free space, in addition to it's successive positions. This would require a Doppler effect analysis to estimate the received signal's frequency. Essentially a correlation between the received signals and multiple matched filters at various frequencies would need to be performed. The matched filter with the highest output would then, with great certainty, reveal the shifted frequency of the reflected signal and consequentially determine the target's velocity. Another complementary and interesting subject would be an assessment on how to estimate the actual shape and geometry of the detected target and what would it take for a ground-based radar to effectively accomplish it. Apparently, a model that extrapolates an object shape into an ellipsoid figure instead of an estimated spherical diameter (such as what the exemplified SEM executes) works better. In this model, the ratio between the number of small and large RCS values split by the mean RCS value is equal to the ellipsoid's curvature providing a greater accuracy in target size estimation.[37] Ultimately, an actual implementation of the projected system in the real-world would be the most desired outcome of a future project given the excitement of dealing hands on with apparatus. The latest advances in semiconductors also seem promising for a powerful development of radar performance. Thanks to the latest GaN technology, transistors can now operate at much higher voltages and at much higher temperatures, making them ideal for high frequency and high efficiency applications such as those required for radar systems. Well-known advantages include an increased frequency availability, a radio frequency reliability at a higher channel temperature as well as an extended product lifetime. A revolutionary enhancement for military radar, electronic warfare and communications applications currently expanding into the commercial market.

However vast and empty outer space may be, the near-Earth space environment is not an infinite resource. With the quick development and regular deployment of smaller and increasingly more accessible technologies such as CubeSats[1], the useful space environment is quickly filling up. To be able to continue operating and benefiting from satellites and space based instruments orbiting around our planet, plans need to be made ahead. The space environment must be taken care of to ensure the future growth and sustainability of mankind.

[1] A type of miniaturized space research satellite weighing no more than 1.33 kilograms. Over 800 have already been launched since April 2018.

Bibliography

[1] ESA's annual space environment report. Technical Note 2, ESA Space Debris Office, May 2018.

[2] ESA's Space Debris Office. About space debris. `https://www.esa.int/Our_Activities/Operations/Space_Debris/About_space_debris`, February 2018.

[3] Nadav Levanon. *Radar Principles*. John Wiley & Sons, 1988.

[4] Christian Wolff. Radar basics. `http://www.radartutorial.eu/index.en.html`, 1998.

[5] M. F. Horstman, V. O. Papanyan, J. A. Hamilton, and Q. Juarez. Haystack and HAX Radar Measurements of the Orbital Debris Environment: 2006-2012. Lyndon B. Johnson Space Center, Houston Texas, 77058, May 2014.

[6] C. L. Stokely, J.L. Foster, E. G. Stansbery, J.R. Benbrook, and Q. Juarez. Haystack and HAX Radar Measurements of the Orbital Debris Environment: 2003. Lyndon B. Johnson Space Center, Houston Texas, 77058, November 2006.

[7] Domingos Barbosa. Survey radar telescope. Private Communication, 2018.

[8] Latest report on space junk. `http://www.esa.int/Our_Activities/Operations/Latest_report_on_space_junk`, July 2018.

[9] S. Montebugnoli, G. Pupillo, E. Salerno, S. Pluchino, and M. di Martino. The bistatic radar capabilities of the Medicina radiotelescopes in space debris detection and tracking. *Advances in Space Research*, 45:676–682, March 2010.

[10] M. Di Martino, S. Montebugnoli, G. Cevolani, S. Ostro, A. Zaitsev, S. Righini, L. Saba, S. Poppi, M. Delbò, A. Orlati, G. Maccaferri, C. Bortolotti, A. Gavrik, and Y. Gavrik. Results of the first italian planetary radar experiment. *Planetary and Space Science*, 52:325–330, 2004.

[11] L. Saba, M. Di Martino, M. Delbò, A. Cellino, V. Zappalà, S. Montebugnoli, S. Righini, L. Zoni, R. Orosei, F. Tosi, G. Valsecchi, A. Gardini, D. Grassi, A. Rossi, A. Milani, and M. Lazzarin. The Sardinian Radio Telescope as Radar for the study of near-Earth Objects and Space Debris. *Memorie della Societa Astronomica Italiana Supplementi*, 6:104–109, 2005.

[12] T. Donath, T. Schilknecht, P. Brousse, J. Laycock, T. Michal, P. Ameline, and L. Leushacke. Proposal for a european space surveillance system. In D. Danesy, editor, *Proceedings of the 4th European Conference on Space Debris, Darmstadt, Germany*, pages 31–38. European Space Agency, 2015.

[13] ESA's Space Debris Office. Space smash: Simulating when satellites collide. https://www.esa.int/Our_Activities/Preparing_for_the_Future/Discovery/Space_smash_simulating_when_satellites_collide, April 2018.

[14] ESA's Space Debris Office. Space debris by the numbers. https://www.esa.int/Our_Activities/Operations/Space_Debris/Space_debris_by_the_numbers.

[15] ESA's Space Debris Office. Space debris environment statistics. https://discosweb.esoc.esa.int/web/guest/statistics;jsessionid=b8b363050bfb56400d33a7f4817e, 2018.

[16] David W. Walsh. A Survey of Radars Capable of Providing Small Debris Measurements for Orbit Prediction. 2013.

[17] ESA's Space Debris Office. Space situational awareness. http://www.esa.int/Our_Activities/Operations/Space_Situational_Awareness/Space_Surveillance_and_Tracking_-_SST_Segment.

[18] Laurent Sacco. La poussière spatiale peut tuer des satellites en formant du plasma, March 2013. https://www.futura-sciences.com/sciences/actualites/astronautique-poussiere-spatiale-peut-tuer-satellites-formant-plasma-44961/.

[19] J. C. Liou. Highlights of recent research activities at the NASA Orbital Debris Program Office. In T. Flohrer and F. Schmitz, editor, *Proceedings of the 7th European Conference on Space Debris*, 2101 NASA Parkway, Houston, TX 77058, USA, April 2017. ESA Space Debris Office.

[20] NASA Astromaterials Research & Exploration Science. Hypervelocity impact technology. https://hvit.jsc.nasa.gov/shield-development/index.html, 2018.

[21] National Research Council, editor. *Orbital Debris: A Technical Assessment*. Washington, DC: The National Academies Press, 1995.

[22] R. Lambour, T. Morgan, and N. Rajan. Orbital Debris Size Estimation from Radar Cross Section Measurements. *2000 RASSC Paper*, April 2013.

[23] Eun-Jung Choi, Sungki Cho, Jung Hyun Jo, Jang-Hyun Park, Taejin Chung, Jaewoo Park, Hocheol Jeon, Ami Yun, and Yonghui Lee. Performance analysis of sensor systems for space situational awareness. *Journal of Astronomy and Space Sciences*, 34(4):303–313, 2017.

[24] ESA's Space Debris Office. European conference on space debris risks and mitigation. https://www.esa.int/Our_Activities/Operations/Space_Debris/European_conference_on_space_debris_risks_and_mitigation.

[25] Red Atlántica de Estaciones Geodinámicas y Espaciales. RAEGE in VGOS/GGOS. http://raege.morfose.net/en/about-us/raege-in-vgosggos/, 2013.

[26] J. A. López-Fernández, J. Gómez-González, L. Santos, F. Colomer, P. de Vicente Abad, S. García Espada, and R. Bolaño. Status of raege network. In R. Haas and F. Colomer, editors, *23rd European VLBI Group for Geodesy and Astrometry Working Meeting*, page 50. May 2017.

[27] J. Gómez-González, L. Santos, J. A. López-Fernández, and F. Colomer. Status of the Spanish-Portuguese RAEGE project. In R. Haas and F. Colomer, editors, *Proceedings of the 22nd European VLBI Group for Geodesy and Astrometry Working Meeting*, pages 55–58, May 2015.

[28] Mark A. Richards. *Fundamentals of Radar Signal Processing*. McGraw-Hill, 2005.

[29] Bernard F. Burke and Francis Graham-Smith. *An Introduction to Radio Astronomy*. Cambridge University Press, 2nd edition edition, 2002.

[30] Merrill I. Skolnik. *Randar Handbook*. McGraw-Hill, 3rd edition, 2008.

[31] Bindu Bothra, Apurba Rani Panda, Subhasis Pradhan, Md. Ashfaque Hussain, and Dillip Dash. Low rcs target detetion: A review. *Internation Journal of Engineering Trends and Technology*, 45(4):141–148, March 2017.

[32] Asem Melebari, Amit Kumar Mishra, and M. Y. Abdul Gaffar. Comparison of Square Law, Linear and Bessel Detectors for CA and OF CFAR Algorithms. In *IEEE Radar Conference*, pages 383–388, 2015.

[33] Mark A. Richards. Alternative Forms of Albersheim's Equation. https://radarsp.weebly.com/uploads/2/1/4/7/21471216/albersheim_alternative_forms.pdf, June 2014.

[34] Joseph J. Carr and John M. Brown. *Introduction to Biomedical Equipment Technology*. Prentice Hall Professional, 3rd edition, 1988.

[35] A.V. N. R. Sai Shiva, Khaled Elleithy, and Eman Abdelfattah. Improved monostatic pulse radar design using ultra wide band for range estimation. In *Annual Connecticut Conference on Industrial Electronics, Technology & Automation (CT-IETA),*. IEEE, October 2016.

[36] ESA's Space Debris Office. Curbing Space Debris in the Era of Mega-Constellations. http://www.esa.int/Our_Activities/Preparing_for_the_Future/Discovery/Curbing_space_debris_in_the_era_of_mega-constellations, July 2018.

[37] Huang Jian, Wang Zhuang, and Hu Weidong. Space debris size estimation based on new statistical characteristics of radar cross section. In *Proceeding of the 5th European Conference on Space Debris, Darmstadt, Germany*, July 2009.